CO6-1 Contribution of indirect actions to cell lethality in mixed neutron and BPA irradiation

R. Hirayama, Y. Sanada[1], A. Uzawa, M. Suzuki[1], S. Masunaga[1] and S. Hasegawa

National Institutes for Quantum Science and Technology
[1] Institute for Integrated Radiation and Nuclear Science, Kyoto University

INTRODUCTION: Excellent dose distribution in a cell of neutron capture reaction of boron atom induces high relative biological effectiveness. These phenomena are commonly assumed to be an interaction between cells and low energy heavy particles (α and Li) resulting from the boron atom fis-sions in the cells. However, there has been little study done concerning the action of the particles on living cells. We have investigated contributions of indirect actions of radiation in cell killing by heavy ions with radical scavenger that selectively reduces the indirect action [1].

Therefore, it is important that how these mechanisms can be made to clear through a thorough basic research in boron neutron capture therapy is urgently discussed. The main object of this year is to make clear the contribution of indirect action of neutron beam to cell killing using mammalian cells.

EXPERIMENTS: We used HSGc-C5 (JCRB1070, here after call as HSG) cells. HSG cells were grown in Eagle's minimum essential medium supplemented with 10% fetal bovine serum and antibiotics (100 U/ml penicillin and 100 μg/ml streptomycin) under humidified air with 5% CO_2 at 37˚C. The cells were suspended at a density of about 3×10^5 cells/ml. The cells in Polypropylene tubes were irradiated at the remodeled heavy water facility at the KURRI.

Total fluencies of thermal neutron, epithermal neutron and fast neutron were measured by means of gold foil activation analysis. The gamma ray dose including secondary gamma rays was measured with a thermo luminescence dosimeter. Boron concentrations in the cells were taken to be equivalent to those in the medium as reported previously [2].

Three hours prior to irradiation, cells are treated with 25 μg/ml BPA.

After irradiation, cells were seeded in triplicate onto 100 mm (Φ) culture dishes at densities to give approximately 100 colonies per dish. After 14 days of incubation, the colonies were fixed with 10 % formalin solution and stained with 1 % methylene blue in water. Colonies consisting of more than 50 surviving cells were scored.

The contribution of indirect action on cell killing can be estimated from the maximum degree of protection by dimethylsulfoxide (DMSO) [1], which suppresses indirect action by quenching OH radicals without affecting the direct action of neutron beam on cell killing.

RESULTS: The surviving fractions of HSG cells irradiated with 0.335 Gy dose initially increased with increasing DMSO concentration and then plateaued at higher concentrations (Fig.1A). Degrees of protection (DP: $(\ln SF_0 - \ln SF_x)/\ln SF_0$) defined was calculated and plotted as a function of the DMSO concentration (Fig. 1B). Since the curve were upper concave in nature, DP curve was approached saturation as the concentration of DMSO increased. The maximum DP (i.e., saturation level) for DMSO concentrations was 0.30. Namely, the OH radical-mediated indirect action contributions to cell killing by neutron beam was 30%.

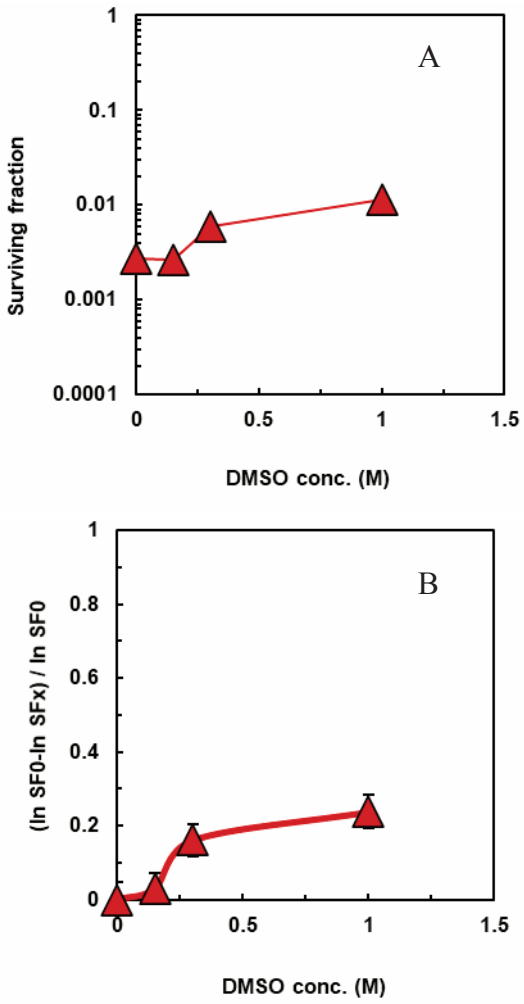

Fig. 1. Effects of DMSO on the survival of HSG cells after exposure to neutron beam. (A) HSG cell survival irradiated with neutron beam in the presence of various concentration of DMSO. (B) Degrees of protections were determined from panel A. The curve was fitted by MichaelisMenten kinetics. The error bars represent the standard errors.

REFERENCES:

[1] R. Hirayama *et al.*, Radiat. Res., **171** (2009) 212-218.
[2] Y. Sakurai and T. kobayashi, Nucl. Instrum. Methods Phys. Res. Sect. A., **453** (2000) 569-596.

CO6-2 The tumor invasion enhanced by the conditioned-medium after X--rays via EGFR pathway

H. Yasui[1], M. Eitaki[1], Y. Sanada[2], S. Masunaga[2], and O. Inanami[1]

[1]*Laboratory of Radiation Biology, Faculty of Veterinary Medicine, Hokkaido University*
[2]*Particle Radiation Biology, Division of Radiation Life Science, Institute for Integrated Radiation and Nuclear Science, Kyoto University*

INTRODUCTION: In cancer studies, it has been suggested that irradiation sometimes enhances invasion of tumor cells. Although there are many studies that estimate effects of direct irradiation on tumor cell invasiveness, not so many reports did bystander effects of irradiated tumor cell conditioned medium (CM) on it. Furthermore. the same effect of high LET radiation therapy such as boron neutron capture reaction (BNCT) has not been reported. In this study, we conducted the experiments to examine effects of X-irradiated tumor cell CM on cellular invasiveness in breast cancer and lung cancer-derived cells, prior to BNCT challenge. In 2018 and 2019, using human breast adenocarcinoma MDA-MB-231 cells and human lung adenocarcinoma A549 cells, we reported the X-ray irradiated ce1l-derived CM promotes cell infiltration ability even if taken into consideration cell proliferation activity and Epidermal growth factor (EGF) acts as a bystander factor to promote the cell invasion ability. [3, 4]. In this year, we examined the effect of EGF suppression on the invasiveness and MMP activity of CM-treated MDA-MB-231 cells.

EXPERIMENTS:
[Western blotting] Cells were treated with CM containing 10% FBS (CM/10 % FBS) for 0, 0.5, 1, 3 or 6 h. When cells were co-treated with AG1478, an EGFR tyrosine kinase inhibitor, they were pre-treated with 500 nM AG1478 for 10 min before treatment of CM/10 % FBS. After the treatment, cells were collected and lysed. Proteins were separated by SDS-PAGE and transferred onto nitrocellulose membranes. The membranes were probed with anti-EGFR, anti-pEGFR. After being probed with HRP-conjugated secondary antibodies, bound antibodies were detected with Western LightningTM Chemiluminescence Reagent Plus kit (Perkin Elmer Life Sciences, Boston, MA, USA).
[In situ gelatin zymography] On cover glasses were covered with 0.178% gelatin and 0.022% fluorescein-conjugated gelatin, cells (2 x 10^5) were suspended in RPMI 1640/10% FBS and seeded. The cells were cultured for 6 hours to adhere to gelatin, the medium was replaced with CM / 10% FBS and the cells were cultured for an additional 18 hours. Cells on the cover glass were fixed with 3.7% paraformaldehyde and permeabilized with 0.5% Triton X-100. F-actin was stained with PBS containing 1% Alexa Fluor 488 phalloidin, and nuclei were further stained with PBS containing 300 nM DAPI. The fluorescence image was taken using an LSM 700 confocal microscope.
RESULTS: To investigate whether X-ray-irradiated cell-derived CM, which has been suggested to increase EGF, promotes cell infiltration through EGFR, the effect of AG1478 on EGFR phosphorylation. EGFR phosphorylation at 3 h of CM treatment was increased in 4 Gy CM treated cells compared to 0 Gy CM treated cells, and this increase was clearly suppressed by AG1478 treatment (Fig. 1A). Furthermore, Cell invasion capacity was increased in 4 Gy CM treated cells, and this increase was significantly suppressed by AG1478 treatment (Fig. 1B). These results suggest that X-ray-irradiated cell-derived CM promotes cell infiltration ability via EGFR. Next, we considered that EGF in CM derived from X-irradiated cells might promote the degradation ability of extracellular matrix via EGFR and examined it by in situ gelatin zymography. As shown in Fig. 2, the gelatin decomposition area per cell was significantly increased in the 4 Gy CM-treated cells. Furthermore, this increase was significantly suppressed by AG1478 treatment. These results suggest that X-ray-irradiated cell-derived CM promotes extracellular matrix resolution via EGFR.

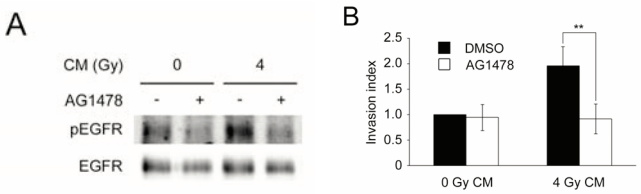

Fig. 1. Involvement of EGFR in promoting cell infiltration induced by X-irradiated cell-derived CM.

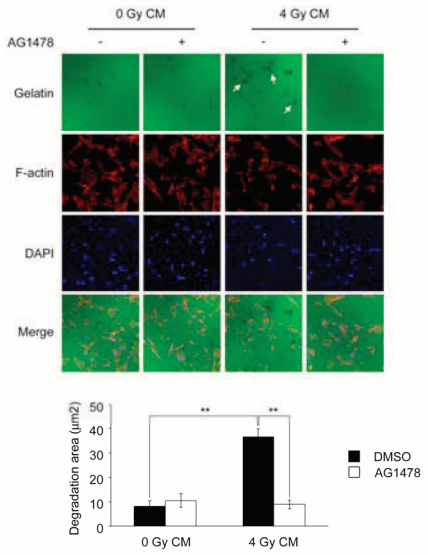

Fig. 2. Effect of CM on the degradation ability of extracellular matrix.

REFERENCES:
[1] H. Yasui *et al.*, KURNS Progress Report 2018, PR8-7.
[2] H. Yasui *et al.*, KURNS Progress Report 2019, PR6-8.

CO6-3 Physicochemical analysis of protein lLEI, which reduces amyloid-β protein production

E. Hibino[1,2], K. Morishima[3], R. Inoue[3], M. Sugiyama[3], and M. Nishimura[1]

[1]*Molecular Neuroscience Research Center, Shiga University of Medical Science*

[2] *Graduate School of Pharmaceutical Sciences, Nagoya University*

[3]*Institute for Integrated Radiation and Nuclear Science, Kyoto University*

INTRODUCTION: Although the number of patients with Alzheimer's disease in Japan continues to increase, no effective disease-modifying drugs have been developed until now. Alzheimer's disease is hypothesized to be caused by the excessive accumulation of amyloid-β protein (Aβ) in the brain, and we have previously discovered that the secreted protein ILEI reduces Aβ production by a specific pathway [1]. After secreted extracellularly, ILEI binds to the extracellular region of presenilin-1, one of the components of the γ-secretase complex. Although the details are currently unknown, this binding promotes nonspecific proteolysis of the Aβ precursor protein, the substrate of γ-secretase, and suppresses Aβ production. However, the structural mechanisms involved in the binding are still unknown. More recently, the X-ray crystal structures of monomeric and dimeric forms of ILEI have been reported [2], but the relationship between the monomeric and dimeric forms and their functions is not clear. These structural aspects are critical issues for Alzheimer's disease drug development.

The objective of this study is to clarify the relationship of ILEI dimers to the inhibitory function of Aβ production and to elucidate the molecular mechanism of ILEI.

EXPERIMENTS: The wild-type and C185A mutant of ILEI (55-227)-His was produced in an E. coli expression system and purified by Ni-NTA resin and size exclusion chromatography (SEC). SDS-PAGE and SEC in the non-reducing state confirm that they are a single band and a single peak, respectively. To compare the properties of wild-type and mutant forms, they were analyzed by analytical ultracentrifuge (AUC). The measurement temperature was 25°C and the rotational speeds were 60,000 rpm. To evaluate the function of Aβ production, plasmids encoding APP-CTF and control vectors or plasmids encoding ILEI (wild-type or C185A mutant) were co-transfected into ILEI knock-out HEK293 cells, and the supernatant was quantified using an ELISA kit (Human Amyloidβ (1-40) Assay Kit, IBL).

RESULTS: One of the functions of ILEI is oncogenesis, which is reported to be inhibited by the replacement of Cys185 with Ala [2]. We thus identified differences in physical properties to clarify the relationship between the C185A mutation and the inhibitory function of Aβ production.

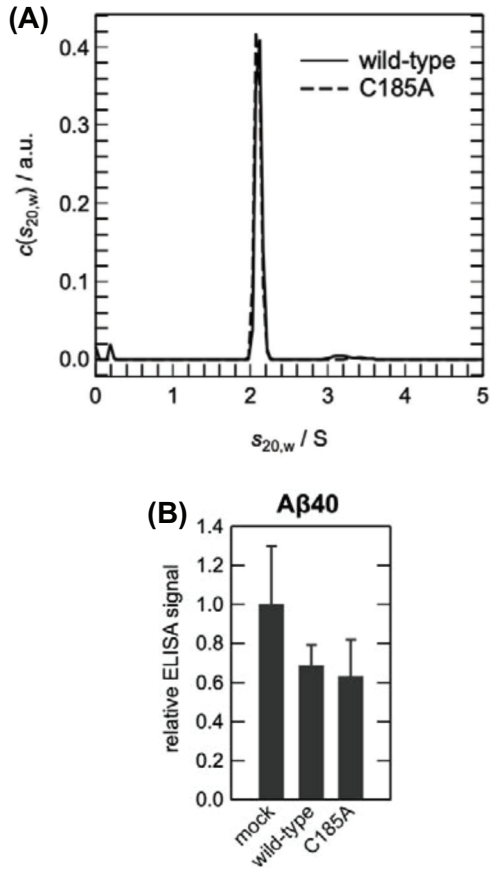

Fig. 1 **A**, Results obtained from analytical ultracentrifugation for wild-type and C185A mutant of ILEI.
B, Quantitation of Aβ40 by ELISA.

First, the configuration of the wild-type and C185A mutants was analyzed by AUC, but no significant differences were observed (Fig. 1A). In addition, the amount of Aβ was quantified by ELISA to analyze the inhibitory function of Aβ production. As a result, it was found that C185A has the same ability to inhibit Aβ production as wild-type (Fig. 1B). These results mean that the inhibitory function of ILEI in the production of Aβ and oncogenesis were found to be exhibited by completely different mechanisms. This is an important finding for the development of ILEI-based drugs for Alzheimer's disease.

REFERENCES:

[1] H. Hasegawa, L. Liu, I. Tooyama, S. Murayama and M. Nishimura, Nat. Commun., **5** (2014) 3917.

[2] M. Kral, C. Klimek, B. Kutay, G. Timelthaler, T. Lendl, B. Neuditschko, C. Gerner, M. Sibilia and A. Csiszar, The FEBS Journal, **284** (2017) 3484–3505.

CO6-4 Solution scattering approach for dynamics of Lys48-linked tri-ubiquitin chain

M. Yagi-Utsumi, M. Hiranyakorn, K. Kato, A. Okuda[1], K. Morishima[1], R. Inoue[1], and M. Sugiyama[1]
Exploratory Research Center for Life and Living Systems (ExCELLS) and Institute for Molecular Science (IMS), National Institutes of Natural Sciences
[1]Institute for Integrated Radiation and Nuclear Science, Kyoto University

INTRODUCTION: Ubiquitin (Ub) molecules can be enzymatically connected through a specific isopeptide linkage, thereby mediating various cellular processes by binding to Ub-interacting proteins through their hydrophobic surfaces. The Lys48-linked Ub chains, which serve as tags for proteasomal degradation, undergo conformational interconversions between open and closed states, in which the hydrophobic surfaces are exposed and shielded, respectively. Previously, we provided a quantitative view of such dynamic processes of Lys48-linked triUb chain in solution [1]. The native and cyclic forms of Ub chains are prepared with isotope labeling by in vitro enzymatic reactions. Our comparative NMR analyses using monomeric Ub and cyclic diUb as reference molecules enabled the quantification of populations of the open and closed states for each Ub unit of the native Ub chains (Fig. 1). The data indicated that the most distal Ub unit in the Ub chains was the most apt to expose its hydrophobic surface, suggesting its preferential involvement in interactions with the Ub-recognizing proteins. We also demonstrated that a mutational modification of the distal end of the Ub chain could remotely affect the solvent exposure of the hydrophobic surfaces of the other Ub units.

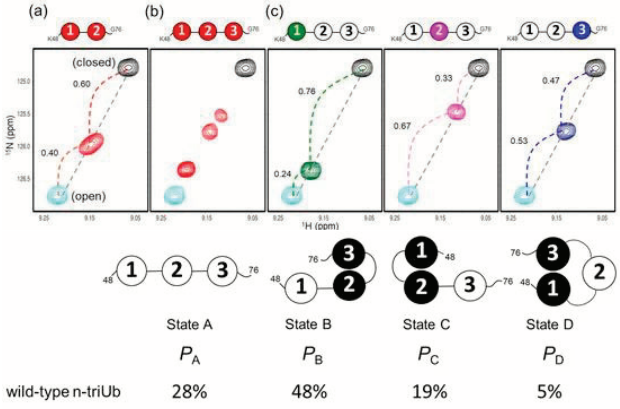

Fig. 1. (Upper) ^{1}H-^{15}N HSQC peaks originating from Val70 of (a) uniformly ^{15}N-labeled diUb (red), (b) uniformly^{15}N-labeled triUb (red), (c) unit-selectively ^{15}N-labeled triUb chains at the distal Ub1 (green), the middle Ub2 (magenta) and the proximal Ub3 (blue). (Lower) Cartoon model of the conformational equilibrium of n-triUb. The populations of states A, B, C, and D of n-triUb are denoted as P_A, P_B, P_C, and P_D, respectively.

Small-angle neutron scattering (SANS) and small-angle X-ray scattering (SAXS) are powerful techniques for the structural characterization of biomolecular complexes. In particular, neutron spin echo (NSE) measurement enables a direct observation of coupled internal protein dynamics. Here, we attempted to elucidate the time scale of the transit domain motions of the Lys48-linked triUb chain as a feasibility study of NES collaborated with SAXS and molecular dynamics (MD) simulation.

EXPERIMENTS: We prepared the Lys48-linked triUb in D_2O solution (5mL, 10mg/ml). We had measured NSE of Lys48-linked triUb at NCNR, NIST. We also performed SEC-SAXS of Lys48-linked triUb chain using the laboratory-based SAXS instruments (NANOPIX, Rigaku).

RESULTS: We firstly performed SEC-SAXS of Lys48-linked triUb chain. As shown in Fig. 2, the experimental SAXS profile (blue marks) showed disagreement with that calculated one (red line) from crystallographic data (State D in Fig. 1). This result strongly supported that the dynamical conformational interconversions revealed by NMR experiments were also observed in SAXS data. Then, we measured NSE of Lys48-linked triUb at the two temperatures of 10 and 42 degrees. An incident neutron wavelength of 6 and 8 angstroms was used to cover fourier times up to 20 ns in a q-range from 0.06 to 0.22 inverse angstroms. Intermediate scattering functions for both states were successfully obtained. The effective diffusion constants (D_{eff}) were obtained by exponential fittings at each q. D_{eff} should include translational and rotational diffusion as well as internal domain motions. The experimentally obtained D_{eff}s are consistent with the MD simulation derived ones at 10 degrees. Based on these results, the contribution of the internal motions can be estimated. The analysis on the temperature dependence of the internal dynamics is on progress. We are trying to analyze the NSE data combined with computational analysis to observe the functional domain motions of Lys48-linked triUb.

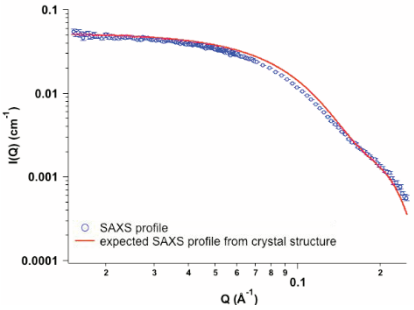

Fig. 2. SAXS of Lys48-linked triUb. Blue marks and red line show experimental and calculated data, respectively.

REFERENCE:
[1] M. Hiranyakorn *et al.*, *Int. J. Mol. Sci.* **21**, 5351 (2020). DOI: 10.3390/ijms21155351.

CO6-5 Radioresistance Mechanisms Acquired by Adaptive Evolution and their Evolutionary Mechanisms II

T. Saito

Institute for Integrated Radiation and Nuclear Science, Kyoto University

INTRODUCTION: In nature, organisms have evolved diversely by adapting to various environmental conditions, some of which can survive in extremely severe environments. Elucidating the mechanisms by which organisms adapt to such severe environmental conditions can provide meaningful information on evolution and biological diversity. Some bacteria, known as radioresistant bacteria, demonstrate extreme resistance to ionizing radiation [1]. The extreme resistance mechanism of these bacteria to ionizing radiation is an interesting area of research from the standpoint of adaptive mechanisms employed by organisms in nature. In order to elucidate the mechanisms of radioresistance in these organisms, their biological defense mechanisms against external stress must be investigated at the molecular level. However, studies on naturally-occurring radioresistant organisms are particularly challenging owing to the limited knowledge of their genetic and biochemical properties. Therefore, in this study, radioresistant *Escherichia coli*, the wild-type genetic and biochemical characteristics of which have been elucidated in detail, were generated by an adaptive evolution experiment using gamma rays as the selective pressure, and the characteristics of the evolved radioresistant *E. coli* were compared with those of the wild-type. A previous reports of this study described the generation of radioresistant *E. coli* with a 7.9-fold resistance compared with that of wild-type *E. coli* [2, 3]. A significant increase in the expression of genes involved in SOS response, response to stimulus, DNA repair, and DNA metabolism (described as anti-stress genes in the text) in radioresistant *E. coli* compared with wild-type *E. coli* under constitutive conditions was observed. This report describes differences in gene expression status between wild-type and radioresistant *E. coli* following gamma irradiation.

EXPERIMENTS: Gamma irradiation and RNA sequencing: Wild-type and radioresistant *E. coli* cells were grown in LB medium at 37°C and 200 rpm to the early log phase. Twenty milliliters of the culture medium was centrifuged at 2000 × *g* at 20°C for 20 min. The supernatant was removed, and the pellet was suspended in 5 mL of PBS (–). Wild-type and radioresistant *E. coli* cell suspensions were irradiated with gamma rays at a 33% survival dose (65 Gy and 420 Gy, respectively) at a dose rate of 22 Gy/min at 20 ± 3°C. The irradiated *E. coli* cell suspension was added to 200 mL of LB medium and incubated at 37°C and 200 rpm for 2 h. The resulting *E. coli* cell suspension was centrifuged at 4000 × *g* at 4°C for 10 min, and the supernatant was removed to obtain a pellet. Total RNA extraction from the resulting pellet and RNA sequencing were performed according to previously reported methods [3].

Analysis of gene expression status: In the analysis, gene expression data with "fragments per kilobase of exon per million reads mapped" values less than 1 for all samples from the two groups compered were filtered out to eliminate noise data. Genes differentially expressed in radioresistant *E. coli* compared with those in wild-type *E. coli* were identified by Welch's t-test and correction for multiple testing using the Benjamini and Hochberg method (BH method) [4]. In addition, Gene Ontology (GO) analysis for the differentially expressed genes (DEGs) in radioresistant *E. coli* was performed using the Database for Annotation, Visualization and Integrated Discovery bioinformatics resources ver.6.8.

Statistical analysis: Welch's t-test and BH method were used to identify DEGs among many genes, and a q-value of less than 0.05 was considered statistically significant. The Expression Analysis Systematic Explorer score was used to test for significance in the GO analysis, and a P-value of less than 0.05 was considered statistically significant [5].

RESULTS: No significant differences were observed in anti-stress gene expression between the non-irradiated and gamma-irradiated wild-type *E. coli*. In contrast, comparing non-irradiated and gamma-irradiated radioresistant *E. coli*, the expression levels of anti-stress genes were significantly increased in gamma-irradiated radioresistant *E. coli*. Furthermore, in a comparison between gamma-irradiated wild-type and gamma-irradiated radioresistant *E. coli*, the expression levels of anti-stress genes in the radioresistant *E. coli* were significantly higher than that in the wild-type *E. coli*. These results strongly suggest that the radiation induction of genes involved in cell recovery, DNA repair, cell survival, and stress response is involved in the mechanism of high radioresistance in the evolved radioresistant *E. coli*.

REFERENCES:

[1] T. Saito, Viva Origino, **30** (2007) 85–92.
[2] T. Saito, KURNS ProgressReport 2019 (2020) 211.
[3] T. Saito, KURNS ProgressReport 2020 (2021) 162.
[4] Y. Benjamini and Y. Hochberg, J. R. Statist. Soc. B, **57** (1995) 289–300.
[5] D. W. Huang *et al.*, Nat. Protoc. **4** (2009) 44–57.

CO6-6 Oligomeric structural transition of HspB1 from Chinese hamster

N. Kurokawa, R. Midorikawa, M. Nakamura, K. Noguchi[1], K. Morishima[2], R. Inoue[2], M. Sugiyama[2] and M. Yohda
Department of Biotechnology and Life Science, Tokyo University of Agriculture and Technology
[1]Instrumentation Analysis Center, Tokyo University of Agriculture and Technology
[2]Institute for Integrated Radiation and Nuclear Science, Kyoto University

INTRODUCTION: HspB1 is a mammalian small heat shock protein that is ubiquitously expressed in almost all tissues and involved in regulating many vital functions. Previously, we analyzed the oligomeric structure of HspB1 from CHO cells (CgHspB1) by size exclusion chromatography with multiangle light scattering (SEC-MALS) and small-angle X-ray scattering (SAXS). The results suggested that CgHspB1 has a 16-mer structure [1]. However, the molecular architecture of HspB1 is controversial. Recently, the crystal structure of human HspB1 was reported [2]. Twenty-four monomers form the oligomeric complex of human HspB1 in a spherical configuration. Each monomer is constructed of a structurally conserved α-crystallin domain exhibiting a 6-stranded beta-sandwich as previously described with mobile N- and C-termini. These results suggest the oligomeric structure of HspB1 changes with the conditions, such as temperature or concentration. This study examined the oligomeric structural change of CgHspB1 by sedimentation velocity analytical ultracentrifugation (SV-AUC).

EXPERIMENTS: Wild-type CgHspB1 and the phosphorylated mimics CgHspB1 and CgHspB1S15D were expressed in *E. coli* using a pET23b vector. They were purified by anion exchange chromatography using TOYOPEARL DEAE-650, RESOURCE Q column, and gel filtration chromatography using Superdex 200. The size of the oligomer structure under various temperature conditions was examined by analytical ultracentrifugation (AUC).

RESULTS: Figure 1 shows the SV-AUC results of CgHspB1 wild type (CgHspB1WT) depending on the temperature and concentration. At a low temperature of 4 °C, CgHspB1 exists as an 18-mer, probably a trimeric complex of hexamers. It is relatively unstable and partially dissociates into small oligomers, hexamers, and dodecamers. At elevated temperatures, the 24-mer was more stable than the 18-mer. The 24-mer is also in dynamic equilibrium with the dissociated oligomers in the hexameric unit. The hexamer further dissociates to dimers. Previously, we showed that a phosphorylation mimic mutant of CgHspB1 with the replacement of Ser15 with Asp (CgHspB1S15D) exhibited relatively lower oligomer stability and more remarkable chaperone activity than the wild type [1]. In AUC-SV, the CgHspB1S15D mutant showed almost identical results as CgHspB1WT. Although we expected to observe more dissociated conformers in CgHspB1S15D at 40 °C, there was virtually no difference. To elucidate the role of the disulfide bond, we examined the effect of dithiothreitol (DTT) on the oligomer conformation of CgHspB1WT at 40 °C. At a low concentration of 0.05 mg/mL, the large oligomer of CgHspB1WT almost wholly dissociated into small oligomers. They seem to be dimers, hexamers, dodecamers, and 18-mers without DTT. In the presence of DTT, the proportion of dimers increased, suggesting that disulfide bonds between dimers partially stabilize hexamers.

CONCLUSION: Our results suggest the following conformational transition model. At a low temperature of 4 °C, CgHspB1 exists as an 18-mer, probably a trimeric complex of hexamers. It is relatively unstable and partially dissociates into small oligomers, hexamers, and dodecamers. At elevated temperatures, the 24-mer was more stable than the 18-mer. The 24-mer is also in dynamic equilibrium with the dissociated oligomers in the hexameric unit. The hexamer further dissociates to dimers. The disulfide bond between conserved cysteine residues seems to be partly responsible for stabilizing hexamers.

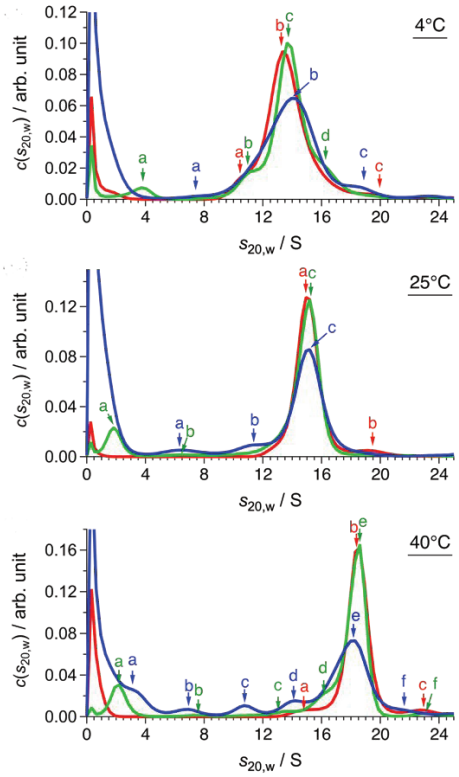

Fig. 1. SV-AUC results of CgHspB1 WT at 4 °C, 25 °C, and 40 °C. Red, green, and blue lines represent c(*s20,w*) at 1.5 mg/mL, 0.5 mg/mL, and 0.1 mg/mL, respectively.

REFERENCES:
[1] E. Sha *et al.*, FEBS Open Bio., 9 (2019) 1826–1834.
[2] L. Nappi *et al.*, J. Clin. Invest. 130 (2020) 699–714.

CO6-7 Study of Ku recognition to a DNA DSB end induced by ionizing radiation

K. Akamatsu[1], N. Shikazono[1] and T. Saito[2]

[1]*Institute of Quantum Life Science, National Institutes for Quantum and Radiological Science and Technology (QST)*
[2]*KURNS*

INTRODUCTION:

DNA lesions induced by ionizing radiation and chemicals can cause mutation and carcinogenesis. In particular, complex double strand break (DSB), having a few base lesions near the end, is believed to hardly be repaired. This damage would be induced around high-LET ionizing radiation tracks. In fact, evidence is found in the direct observation by AFM (atomic force microscopy) [1]. However, the reason why the complex DSBs are unrepairable is unknown. A possible hypothesis is that a repair system by non-homologous end joining (NHEJ), initiated by recognition of DSB end by Ku70/80 heterodimer (Ku), is unsuccessful due to a complex DSB end. In this study we investigate the affinity of Ku-DSB complex and possible formation of Ku-DSB covalent crosslinking using a real DSB end induced by irradiation as well as a model DSB end. Abundant DNA fragments with DSB are needed for this study.

EXPERIMENTS:

●*Sample preparation and irradiation*

The supercoiled plasmid DNA was used as a sample for the study. The DNA was dissolved to be ~10 mg/mL in 0.2 M Tris-HCl buffer (pH 7.5) which is a cell-mimetic condition in relation to radical scavenging capacity. Eight microliters of the DNA solution were transferred to a glass plate (10 mmϕ) under 100 % RH at r.t., and was irradiated with heavy ion beams at TIARA and HIMAC (QST), and ^{60}Co γ-rays (LET: ~0.3 keV/μm; KURNS) as a standard radiation source. Each of irradiated DNA samples was divided into a few aliquots and purified by ethanol precipitation, followed by being dried in vacuum. The dry samples were kept at -20°C until use.

●*Isolation of linear-formed fragment from irradiated pUC19 by agarose gel electrophoresis*

The irradiated DNA pellet was dissolved in 80 μL of 0.5 x TBE buffer at pH 8 with loading dye solution. The DNA sample solution was applied to several wells on an agarose gel. After electrophoresis (25V, 18h at 4 °C), one lane was cut out by a scalpel and was stained by ethidium bromide, which is used as a marker gel to isolate a band containing linear-formed fragment from the other lanes. The stained marker gel was reset on the original gel, and the bands containing the DNA with DSBs were collected using an illuminator equipped with a visible light excitation system. The obtained gel fragments were set into D-Tube Dialyzer to isolate the DNA fragments from the gel by electrophoresis (120V, 4 °C, 1h).

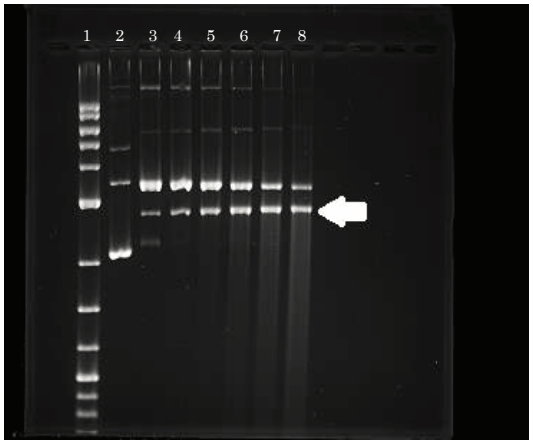

Fig. 1. The image of agarose gel electrophoresis of γ-irradiated pUC19. The gel was stained by ethidium bromide. Lane1: 0.1-10kbp 2-log ladder marker, lane2: non-irradiated control (supercoiled form), lane3: 1kGy, lane4: 2kGy, lane5: 3kGy, lane6: 5kGy, lane7: 7kGy, lane8: 10kGy. The arrow indicates linear formed DNA fragments. The upper bands than the arrow indicate those of the open circular DNA, induced by a single strand break formation on a supercoiled DNA.

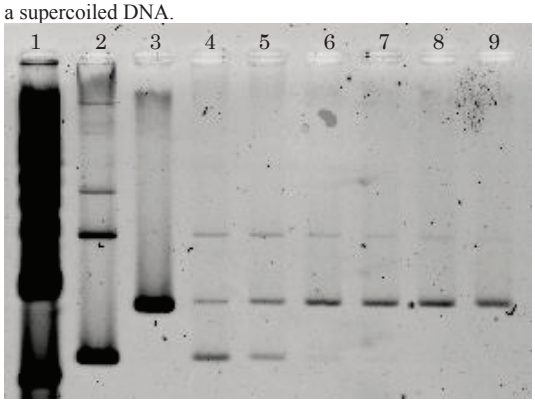

Fig. 2. The image of agarose gel electrophoresis of isolated linear-formed pUC19 fragments induced by γ-irradiation. The gel was stained by ethidium bromide. Lane1: 0.1-10kbp 2-log ladder marker, lane2: non-irradiated control, lane3: pUC19 digested by Sma I, lane4: 1kGy, lane5: 2kGy, lane6: 3kGy, lane7: 5kGy, lane8: 7kGy, lane9: 10kGy.

RESULTS AND DISCUSSION:

Figure 1 shows an agarose gel image of γ-irradiated pUC19, indicating that the original supercoiled DNA was successively changed to linear formed fragment via open circular form with increasing absorption dose. Figure 2 shows a gel image of samples after isolating linear-formed DNA. At a low dose, supercoild DNA fragments fairly remain, whereas highly-fragmented DNA molecules may be contaminated at a high dose. Consequently, the optical dose at the present irradiation condition is around 3kGy. We have plans to use the isolated DNA substrates for the study of Ku-DSB interaction by means of e.g., electrophoretic mobility shift assay and slot-blot-ELISA.

REFERENCES:

[1] T. Nakano, *et al.*, Proc.Natl.Acad.Sci.USA **119** (2022) e2119132119.

CO6-8 Estimation of trace elements in foods and amounts of intake of wild Japanese macaques

M. Fukushima[1], Y. Tsuji[1], Y. Iinuma[2]

[1]*Faculty of Sciences and Engineering, Ishinomaki Senshu University*

[2]*Institute for Integrated Radiation and Nuclear Science, Kyoto University*

INTRODUCTION: It is important to obtain multi element levels in food samples of wild animals for their conservation. Several reports on behavior observation, nutritional analyses, and estimations of energy and protein intake for wild Japanese macaques (*Macaca fuscata*), endemic species in Japan, have been published [1-3]. Primates need trace elements in addition to basic nutritional terms (e.g., protein and energy) [4], but there have been less information on their intake of trace elements from natural food. Y. Tsuji collected food and feces of wild macaques inhabiting Kinkazan Island, Ishinomaki, Miyagi in 2004-2005. Kinkazan is isolated from main island about 0.7 km away, and there are no residents. Intake of trace elements can be estimated by subtracting amounts of elements in feces from those of food. Also, another approach for estimating intake of trace elements, enzymolysis was applied to food samples.

EXPERIMENTAL: Food samples included leaves, flowers, buds, seeds, barks, nuts of woody plants, seaweeds, shells, insects, leaves of herbaceous plants, and mushrooms. Samples were freeze dried without washing with water, and pulverized. Dried powder of nuts was then dry-ashed for 5.5 hours at 550°C. Feces were kept in 70% ethanol after the collection, and ashed for 2 hours at 600°C after drying ethanol at 60°C.

NAA was done by two different conditions according to nuclides for the interest. 1) One portion of samples was irradiated for 1-1.5 min in TcPn site. After 3 minutes decay, gamma spectrum was measured for 10 minutes by Ge detector with CSS. Levels of Br, Ca, Cl, Cu, I, K, Mg, Mn, Na, and V were analyzed using ^{80}Br, ^{49}Ca, ^{38}Cl, ^{64}Cu, ^{128}I, ^{42}K, ^{27}Mg, ^{56}Mn, ^{24}Na, and ^{52}V. 2) Another portion of samples was irradiated for 1 hour, and gamma spectrum was measured for 20 minutes after 1 month decay for analyzing Ag, Co, Cr, Cs, Fe, Rb, Sc, Se, and Zn using ^{110m}Ag, ^{60}Co, ^{51}Cr, ^{134}Cs, ^{59}Fe, ^{86}Rb, ^{46}Sc, ^{75}Se, and ^{65}Zn, respectively. NAA method used was validated using NIST SRM 1515 Apple Leaves, NIST SRM 1566b Oyster Tissue, SRM 1573a Tomato Leaves, NIST SRM 1575 Pine Needles, and NRCC-TORT-1 Lobster Hepatopancreas.

Enzymolysis was done by stepwise using α-amylase, protease, and amyloglucosidase to 1 g of food sample, after filtrating the residue, ethanol was added to elute for precipitating the water-soluble fiber. Both of residue and water-soluble fiber are thought to be non-bioavailable portion. Thus, intake of trace elements was estimated by subtracting amounts of elements in non-bioavailable portion from total amount of elements in food samples before enzymolysis.

RESULTS: One of results obtained for food sample are shown in Fig. 1 as an example. Concentrations were calculated as average and standard deviation for results (n = 2 ~ 5). Fe concentrations differed much between species of trees. Almost all elemental levels except Se were extremely high comparing to food of human beings.

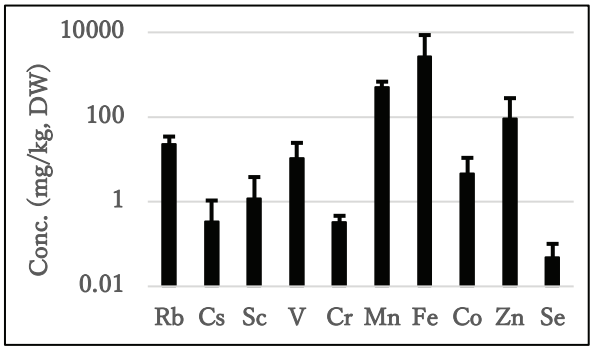

Fig.1 Levels of minor elements in woody leaves (n=2~5) taken by Japanese macaques.

Since Tsuji identified each macaque individual, he could collected fecal samples of identified animals. As an example, we show estimated intake of elements in food and fecal samples for a female individual (body weight: 8 kg) in Table 1.

Table 1 Estimated intake and excretion of elements of one specific female individual of Japanese macaque.

Element	Estimated intake (mg/day)	Excretion (mg/occasion)
Ca	694	233
K	3150	186
Mg	329	64.5
Fe	292	611
Zn	9.9	15.1
Cu	2.4	0.38
Mn	17.7	6.2
I	0.64	Not determined
Se	Not detected	0.36
Cr	0.04	0.88
Rb	5.9	9.4
V	0.44	0.15

The intake did not cover the excretion for Fe, Zn, Cr, and Rb. Further experiments are needed for future for the nutritional information for Japanese macaques.

REFERENCES

[1] Tsuji *et al*., Primates, **49** (2008) 157-160.
[2] Tsuji & Takatsuki, Int. J. Primatol., **33** (2012) 489-512.
[3] Kurihara *et al*., Primates, **61** (2020) 427-442.
[4] National Research Council (National Academic Press) (2003).

CO6-9 Evaluation of radiation resistance of lens constituent proteins involved in age-related cataract

T. Takata[1] and K. Lampi[2]

[1] *Institute for Integrated Radiation and Nuclear Science, Kyoto University*
[2] *Oregon Health & Science University*

INTRODUCTION:
The transparency of the lens is maintained by the stable long-lived protein interactions, comprising α-, β-, and γ-crystallin families. A kind of intrinsic damages of lens tissues, such as heat damage, is increased with time. On the other hand, extrinsic damages, such as UV damage, strongly depends on the living environment in the world. Lens contains various protection systems to prevent UV-inducing oxidative stress; however, damaged proteins can still accumulate because these protection systems are lost with aging. The damaged crystallin species have been further subjected to the additional covalent modifications of amino acid residues levels [1]. Those modifications, which are generated by UV light, ionizing irradiation and oxidative stress, are believed lead to the development of age-related cataracts. There are many data on the oxidation "sites" of aged human lens crystallin species, but there are few studies of the oxidation "effects" for each amino acid residue in crystallin. One of oxidative stress inducer, γ-Irradiation generates free radicals and reactive oxygen species (ROS) such as hydroxyl radicals, superoxide, and singlet oxygen, which have been predicted to induce the oxidation of amino acids, as well as the truncation and cross-linking of proteins. Due to COVID-19, the preparation of mouse lens and the timing of irradiation experiment did not match. So, we used our stock aged human lens for targeting the oxidation "sites" for mass spectrometry. As a result, we could find out the oxidation "sites" in human lens βB2-crystallin. The further aim of this study was to investigate that effect of oxidation for βB2-crystallin stabilities.

EXPERIMENTS:
Material Lens from 79 years old was homogenized and fractionated by centrifugation to isolate lens water soluble (WS) fractions. The WS proteins were dissolved and applied for trypsin digestion as previously reported [2]. Recombinantly expressed lens βB2-crystallin wild-type (WT) were prepared and purified as described previously [3]. *In vivo* oxidation candidate sites in βB2-crystallin were mimicked by replacing Tryptophan residues (W) into Phenyl alanine (F) residues by using a QuikChange Mutagenesis kit (Stratagene). The purification was performed as WT.
LC-MS analysis The tryptic peptides from aged lens WS were filtered and injected into LC-MS/MS for modification analysis as previously reported [2]. The oxidation was screened using by Proteome Discoverer™ 1.0 software (ThermoFisher, USA).
CD analysis Circular dichroism measurements in the far-UV range (far-UVCD) were obtained by using a J-810 spectropolarimeter (JASCO, Tokyo, Japan). For far-UVCD, 0.3 mg/mL of protein sample was prepared, and measured in a cell with a 0.1-cm path length.

RESULTS:
The database search for oxidation of amino acid residues in 79 years old lens showed many modifications in crystallin species. The heavily oxidation of W151 was detected in βB2-crystallin (Fig. 1). There was also heavily acetylation of N-terminal of each protein (data not shown). These data were similar with our previous results that increasing oxidation of tryptophan residues on the βB2-crystallin after γ-Irradiation.

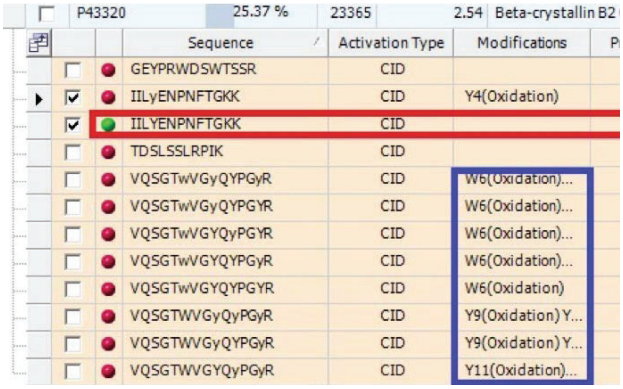

Fig. 1. Heavily Oxidation of Trp151 in human βB2-crystallin from aged lens.

Next, to investigate the significance of tryptophan residues in βB2-crystallin, four βB2-crystallin mimic proteins were prepared (wild type, W82F, W85F, and W151F). The CD analysis for four out of four mimics indicated no structural alteration of secondary structure (Fig. 2).

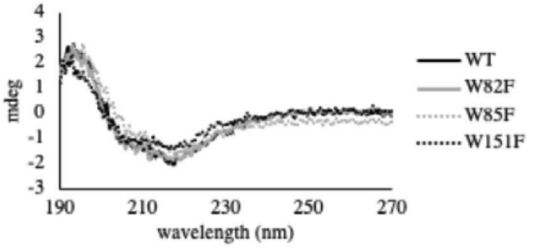

Fig. 2. CD analysis for all βB2-crystallin mimics.

Since the structural differences between W and F is small, the effect for the secondary structure maybe little. However, loss of indole ring should be critical for oxidative stress. To see these effect, βB2-crystallin mimics would be used for γ-irradiation assay.

REFERENCES:
[1] B. Searle *et al.*, *J Proteome Res*, **4** (2005) 546-554.
[2] N. Fujii *et al.*, J. Biol Chem., **287** (2012) 663-669.
[3] K. Lampi *et al.*, *Biochemistry.* **45** (2006) 3146-3153.

CO6-10 Asp racemization/isomerization in shedding products of cell adhesion molecule 1 is potentially involved in the neurodegeneration induced by elevated pressure

A. Yoneshige[1], A. Ito[1] and T. Takata[2]

[1]*Department of Pathology, Kindai University*
[2]*KURNS*

INTRODUCTION: The elevation of internal pressure is often involved in neurodegeneration; intraocular and intraventricular pressure elevations over 20–30 cmH_2O cause glaucoma and hydrocephalus, respectively.
Previously, to investigate the mechanisms by which elevation of intraluminal pressure causes cell or tissue degeneration, we devised a novel two-chamber culture system that enabled us to subject cultured cells to low levels of water pressure (2-50 cmH_2O pressure load) [1,2]. We found that mouse primary neurons degenerated when the water pressure was above 30 cmH_2O, and that ectodomain shedding of synaptic cell adhesion molecule 1 (CADM1) increased in a water pressure-dependent manner [1]. We also discovered that the increase of intracellular product of CADM1 shedding (C-terminal fragment, CADM1-CTF) resulted in decreased neurite density with punctate localization of CADM1 suggesting its aggregation in neurites [1].
CADM1-CTF is rich in Asp residues neighbored by Ala residues, and the conversion of these amino acids to poly-Gly diminished its aggregation state. Since the racemization and isomerization of Asp residues contributes to aggregation of various proteins and it likely occurred when the neighboring residues are small [3,4], these insights led us to hypothesize an involvement of Asp racemization/isomerization in the neurodegeneration induced by internal pressure elevation.

EXPERIMENTS:
(1) Synthetic peptide of internal sequence of CADM1-CTF (GADDAADADTAIINAEGGQNNSEEK) was incubated at 50°C for 0-15 days and applied to LC-MS to identify Asp isomer-containing peptides.
(2) Mouse neuroblastoma cell line Neuro-2a cells with exogenously expressed CADM1-CTF were cultured under 50 cmH_2O and were prepared for LC-MS analysis.
(3) To mimic the human ocular hypertension, mouse retinal explant cultures were prepared to exsert water pressure on to the tissues.

RESULTS:
(1) In LC-MS analysis of CADM1-CTF synthetic peptide, multiple peaks were detected after 1 day at pH 6.0 or pH 7.0 indicating that Asp racemization/isomerization could occurred under neutral pH.
(2) CADM1-CTF proteins in Neuro-2a cells were solubilized with water, Triton X-100 containing buffer, or SDS containing buffer after 3 days culture under 50 cmH_2O, and CADM1 immunoblot was carried out. CADM1-CTF protein yields (CADM1-CTF / total proteins) were in the order Triton X-100 > SDS > water, however, the peptide peak was not identified using with LC-MS. To resolve this problem, future experiments are planned for the isolation of CADM1-CTF from cell extracts by immunoprecipitation with the antibody recognize C-terminal of CADM1.
(3) In retinal explant cultures, since PI-positive necrotic cells have begun to appear after 3 days at atmospheric pressure, the cultured retinae were collected at 2 days *in vitro*. The number of TUNEL-positive apoptotic retinal ganglion cells and the degree of GFAP-positive gliosis were analyzed histologically. Those neurodegenerative features were reproduced experimentally in cultured retinae at 50 cmH_2O. Furthermore, we found that Lipocalin-2, an iron binding protein is involved in retinal degeneration both *in vitro* and *in vivo* [5] (Fig.1). Since iron dysregulation induces oxidative stress, further studies exploring the linkage between oxidative stress and Asp racemization/isomerization are needed.

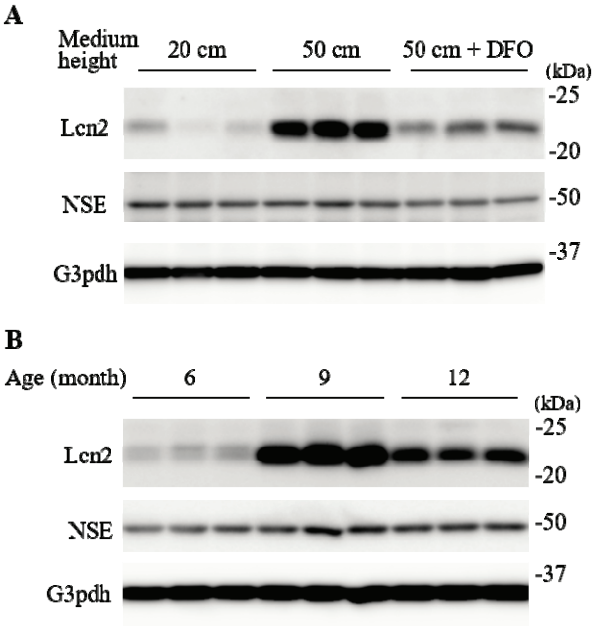

Fig. 1. Lipocalin-2 (Lcn2) upregulation in cultured retinae (A) and in retinae of glaucomatous DBA/2J mice (B). For more information, refer to [5].

REFERENCES:
[1] A. Yoneshige *et al.*, Mol. Neurobiol., **54** (2017) 6378-6390.
[2] M. Hagiyama *et al.*, Front. Physiol., **8** (2017) 997.
[3] N. Fujii *et al.*, J. Biochem., **116** (1994) 663-669.
[4] T. Takata *et al.*, Protein Sci., **29** (2020) 955-965.
[5] A. Yoneshige *et al.*, Front. Cell Dev. Biol., **9** (2021) 664327.

CO6-11 The Study of Boron Neutron Capture Therapy (BNCT) for Primary Central Nervous System Lymphoma (PCNSL)

Hideki Kashiwagi[1], Shinji Kawabata[1],
Kohei Yoshimura[1], Yusuke Fukuo[1], Takuya Kanemitsu[1],
Koji Takeuchi[1], Gen Futamura[1], Ryo Hiramatsu[1],
Tsubasa Watanabe[2], Takushi Takata[2], Hiroki Tanaka[2],
Minoru Suzuki[2], Shin-Ichi Miyatake[3], Koji Ono[3],
Masahiko Wanibuchi[1]

[1] *Department of Neurosurgery, Osaka Medical and Pharmaceutical University*
[2] *Institute for Integrated Radiation and Nuclear Science, Kyoto University*
[3] *Kansai BNCT Medical Center, Osaka Medical and Pharmaceutical University*

Introduction:
Primary central nervous system lymphoma (PCNSL) is classified as WHO grade IV and accounts for 5% of all brain tumors [1, 2]. Standard care of PCNSL is based on high-dose methotrexate (HD-MTX) chemotherapy followed by whole brain radiation therapy (WBRT), and is the widely recommended initial treatment. This tumor responds well to initial therapy, but relapses after successful treatment are causes of poor prognosis due to the lack of safe and effective treatments for relapse; BNCT may be an effective treatment for PCNSL relapse because it is a highly cell-selective particle therapy. Therefore, we conducted basic experiments of BNCT for PCNSL in order to expand the indication of BNCT for the treatment of recurrent / refractory PCNSL.

Materials and Methods:
A CNS lymphoma model was created by inoculating the Raji human lymphoma cell line into the BALB/c nu-nu mice brain, which has been shown to accumulate boron in tumor cells by exposing to BPA in vitro. The boron compound used for all experiments was boronophenylalanine (BPA), which was administered intraperitoneally and the dose was 500mg/kg b.w. (24 mg Boron/kg). The reactor power of the KUR was 1 MW and the irradiation times were 15 or 30 minutes. The mouse CNS lymphoma models were randomly divided into the following 5 groups for neutron irradiation experiments: untreated control group (Untreated), BPA only control group (BPA control), neutron 30 minutes irradiation control group (Irradiated), BPA administration followed by 15 minutes neutron irradiation group (BNCT 15-min), and BPA administration followed by 30 minutes neutron irradiation group (BPA 30-min). The results were analyzed using Kaplan-Meier survival curves and statistical differences are shown using the log-rank test. [3]

Results:
The results of BNCT study for the mouse CNS lymphoma models divided to 5 groups described above were summarized in Table 1., and the Kaplan-Meier survival curves were shown in Fig. 1. The median survival time (MST) for each group were as follows: Untreated; 26.5 days [95% confidence interval (CI); 23.5 – 33 days], BPA control; 31.0 days [95% CI; 24 – 33 days], Irradiated; 31.5 days [95% CI; 28 – 33 days], BPA BNCT-15min; 39 days [95% CI; 35.5 – 48.5 days], BPA BNCT-30min; 44.0 days [95% CI; 37 – days]. There were statistically significant differences between the BPA BNCT 15-min and Untreated ($p = 0.02$) and between the BPA BNCT 30-min group and Untreated ($p = 0.007$). [3]

Table 1. The BNCT result for the CNS lymphoma models

Group	n	MST (days)	95% CI (days)
Untreated	6	26.5	23.5-33.0
BPA control	6	31.0	24.0-33.0
Irradiated	8	31.5	28.0-33.0
BPA BNCT 15-min	7	39.0	35.5-48.5
BPA BNCT 30-min	8	44.0	37-

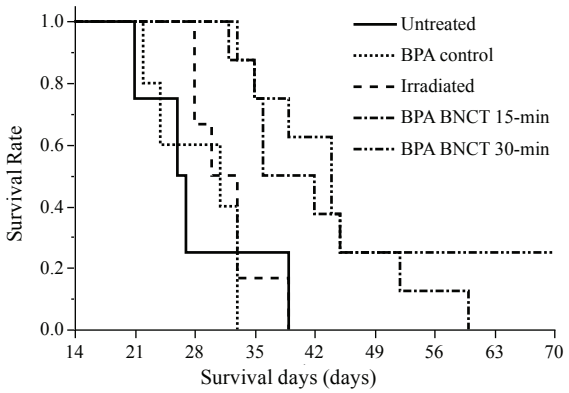

Fig. 1 The Kaplan-Meier survival curves. The BPA-BNCT groups obtained a significant survival advantage over the control group.

Conclusion:
BNCT with BPA was highly effective in an experimental animal model of PCNSL. Some new treatment options for PCNSL are needed and BNCT may be a promising treatment option for PCNSL. The results of this study suggest that future clinical trials exploring the potential of BNCT as a new treatment option for PCNSL may be successful.

References:
[1] Ostrom, Q.T. *et al.,* Neuro Oncol, 21 (2019) v1-v100.
[2] Villano, J.L. *et al.*, Br J Cancer, 105 (2011) 1414-1418.
[3] K.Yoshimura *et al.,* Cells, 10(12) (2021) 3398.

R3057

CO6-12 Evaluation of boron neutron capture therapy (BNCT) using brain tumor bearing rats or mice models

Hideki Kashiwagi[1], Shinji Kawabata[1], Ryo Kayama[1], Kohei Yoshimura[1], Yusuke Fukuo[1], Takuya Kanemitsu[1], Koji Takeuchi[1], Gen Futamura[1], Ryo Hiramatsu[1], Kai Nishimura[2], Kazuki Kawai[2], Takushi Takata[3], Hiroki Tanaka[3], Tsubasa Watanabe[3], Minoru Suzuki[3], Shin-Ichi Miyatake[4], Hiroyuki Nakamura[2], Masahiko Wanibuchi[1]

[1] *Department of Neurosurgery, Osaka Medical and Pharmaceutical University*
[2] *Laboratory for Chemistry and Life Science, Institute of Innovative Research, Tokyo Institute of Technology*
[3] *Institute for Integrated Radiation and Nuclear Science, Kyoto University*
[4] *Kansai BNCT Medical Center, Osaka Medical and Pharmaceutical University*

Introduction:
Boron neutron capture therapy (BNCT), which can be targeted at the cellular level using high-energy particle beams, is a promising treatment for high-grade gliomas (HG). We have demonstrated the BNCT efficacy using maleimide-conjugated *closo*-dodecaborate (MID) bound serum albumin (MID-AC) as a drug delivery system for an F98 rat brain tumor model. MID-AC accumulated in the brain tumor and BNCT using MID-AC produced approximately the same therapeutic effect as BNCT using BPA [1]. Whereas, cyclic RGD peptide is known to bind to integrins that overexpress in many cancer cells including glioma cells. We focused on c(RGDfK), which binds strongly to integrin $\alpha_v\beta_3$. Consequently, the cRGD peptide ligand conjugated serum albumin bound MID (cRGD-MID-AC) has been developed. BNCT using cRGD-MID-AC showed significant tumor growth suppression in the U87MG xenograft subcutaneous tumor models after neutron irradiation [2]. However, the efficacy of BNCT against HG needs to be evaluated in an experimental brain tumor model due to the different nature of subcutaneous and intracerebral tumors, and thus this neutron irradiation experiment was conducted in a rat brain tumor model.

Materials and Methods:
To evaluate the BNCT efficacy at cRGD-MID-AC administration to the rat brain tumor model, an in vivo neutron irradiation experiment was performed at KUR. F98 rat glioma cells and Fischer rats were used and created the F98 rat glioma bearing brain tumor model. The result was analyzed using Kaplan-Meier survival curves. The reactor power of KUR was 5 MW and the irradiation time was 20 minutes. The F98 rat glioma models were randomly divided into the following six groups: untreated control group (Untreated), neutron irradiated control group (Irradiated), neutron irradiation following 2.5 or 8 hours after termination of intravenous administration (i.v.) of BPA (BPA 2.5 h or 8 h), and neutron irradiation following 2.5 or 8 hours after termination of i.v. of cRGD-MID-AC (cRGD-MID-AC 2.5 h or 8 h).

Results:
The treatment effect was evaluated by using Kaplan–Meier survival curves. Each median survival times (MST) was as follows: Untreated; 30.0 days [95% confidence interval (CI); 26–34 days], Irradiated; 35.0 days [95% CI; 22–40 days], BPA 2.5 h; 42.0 days [95% CI; 39–50 days], BPA 8 h; 40 days [95% CI; 34–48 days], cRGD-MID-AC 2.5 h; 43.0 days [95% CI; 32–47 days], and cRGD-MID-AC 8 h; 38.5 days [95% CI; 27– days]. Significant differences were statistically observed between Untreated and all BNCT groups by the log-rank test. At the case of cRGD-MID-AC 8h, one F98 rat glioma model of them still survived for a long time at 90 days after the F98 rat glioma cells implantation when the other groups have completed their observations.

Table 1. The BNCT result for the F98 rat glioma model

Group	n	MST (days)	95% CI (days)
Untreated	5	30.0	26-34
Irradiated	4	35.0	22-40
BPA 2.5 h	6	42.0	39-50
BPA 8 h	5	40.0	34-48
cRGD-MID-AC 2.5 h	7	43.0	32-48
cRGD-MID-AC 8 h	6	38.5	27-

Conclusion:
The addition of tumor directivity to MID-AC appears to have enabled coverage of a large number of tumor cells due to the albumin-based drug delivery system and integrin-mediated tumor directivity. Based on these results, our research team is currently developing further novel boron compounds. We have previously developed boron compounds that target a folate receptor [3], and we intend to introduce further tumor directivity and a drug delivery system to these compounds in order to develop drugs that are more locally concentrated in tumors.

References:
[1] H. Kashiwagi *et al*., Invest New Drugs, 40(2) (2022) 255-264.
[2] K. Kawai *et al.*, Mol Pharm, 17(10) (2020) 3740-3747.
[3] T. Kanemitsu *et al*., Radiat Environ Biophys 58(1) (2019) 59–67.

CO6-13 Establishment of protocol of the prepartion of deuterated protein amied for neutron scattering

R. Inoue, A. Okuda, K. Morishima, M. Shimizu, N. Sato, R. Urade and M. Sugiyama

Institute for Integrated Radiation and Nuclear Science (KURNS), Kyoto University

INTRODUCTION:

One of the noticeable properties associated with neutron scattering is an isotope effect on the neutron scattering length and this effect is especially evident for hydrogen (H). To be more specific, the neutron scattering length of H is significantly different from that of Deuterium (D). Since H atoms are abundantly included in softmatter and biological samples, this property is quite advantageous for studying their structure and dynamics. Let us consider the case for utilization of isotope effect for the structural analysis of protein samples in solution with neutron scattering. The scattering intensity is given by the square of scattering contrast ($\Delta\rho$), which is defined as the difference of neutron scattering length density (SLD) between solute and solvent in the case of biological solution scattering. By setting the value of $\Delta\rho$ to 0, the solute can be "scatteringly invisible". This technique is quite helpful for the structural analyzes of partial concerned component in the multi-component system or complex with neutron solution scattering. To realize high signal to noise ratio of observable scattering profile, the inverse contrast matching SANS (iCM-SANS) method has been proposed and extensively utilized by our group [1-3]. In this method, both partially deuterated (~75%) and hydrogenated protein are prepared in 100% D_2O. Under this solution condition, partially deuterated are "scatteringly invisible" and hydrogenated protein are "scattering visible", respectively. The most important procedure is the preparation of partially deuterated protein. We then try to establish the procedure of preparation of partially deuterated protein, which is fitted for iCM-SANS.

EXPERIMENTS:

We prepared three different lots of partially deuterated αB-crystallin (αB) [3]. The cells are cultured in M9 minimal media containing deuterated glucose (1.5 g/L), hydrogenated glucose (0.5 g/L), autoclaved milliQ (250.0 mL), and 99.8% D_2O (750.0 mL). MALDI-TOF Mass Spectrometry 20 (microflexLT: Bruker Daltonics) was used for the determination of degree of deuteration of prepared partially deuterated protein. To check the quality of partially deuterated protein in terms of "scatteringly invisible", we also performed small-angle neutron scattering measurements on these sample. SANS measurements were performed with QUOKKA installed at the Australian Nuclear Science and Technology Organization (ANSTO, Lucas Heights, NSW, Australia).

RESULTS:

Fig. 1 shows the mass spectra of three different lots of partially deuterated αB (pd-αB) and the degree of deuteration ranged from 70.6 % to 71.7 %. From our preliminary calculation, 73.2% deuterated αB is exactly scatteringly invisible in 100% D_2O solvent. Hence, it is expected that our prepared all three lots of partially deuterated could be nearly "scatteringly invisible" in 100% D_2O. To validate such an expectation, we concentrated all three lots of pd-αB and finally obtained pd-αB at the concentration of 28.5 mg/mL. Fig. 2 shows the SANS profiles from pd-αB at

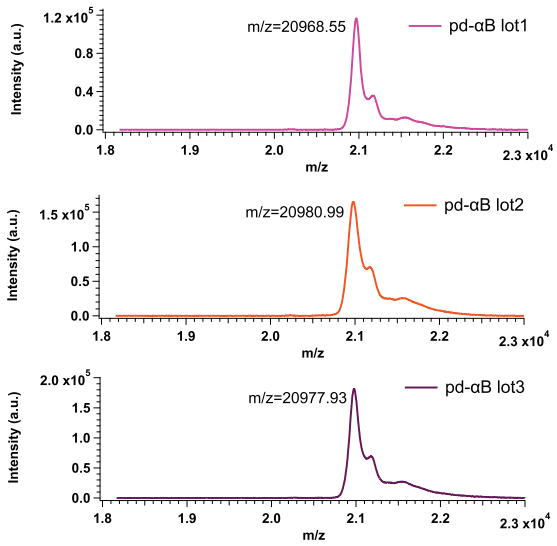

Fig.1 The mass spectra of three different lots of partially deuterated proteins.

28.5 mg/mL and hydrogenated αB (h-αB) at 0.45 mg/mL,

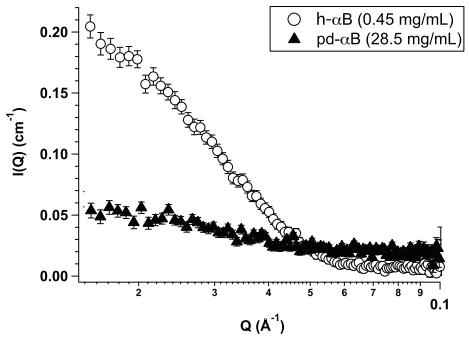

Fig. 2 SANS profiles from partially deuterated αB-cry at 28.5 mg/mL (circle) and hydrogenated αB-cry at 0.45 mg/mL (black triangle).

respectively. Interestingly, the scattering intensity from pd-αB at 28.5 mg/mL is about four time lower than that of h-αB at 0.45 mg/mL. It means that our prepared partially are fulfilled the criteria of "scatteringly invisible" in 100% D_2O even for concentrated protein. It is expected that our protocol would be applicable for other protein samples.

REFERENCES:

[1] M. Sugiyama *et al*., J. Appl. Cryst. **47** (2014) 430–435.
[2] M. Sugiyama *et al*., Sci. Rep. **6**, (2016) 35567.
[3] R. Inoue *et al*., Sci. Rep. **11**, (2021) 2555.

CO6-14 Overall structure of fully assembled cyanobacterial KaiABC circadian clock complex by an integrated experimental-computational approach

H. Yagi[1], Y. Yunoki[1,2,3], K. Morishima[3], A. Matsumoto[4], N. Sato[3], L. Porcar[5], A. Martel[5], R. Inoue[3], H. Kono[4], K. Kato[1,2] and M. Sugiyama[3]

[1]*Graduate School of Pharmaceutical Sciences, Nagoya City University*
[2]*Exploratory Research Center on Life and Living Systems, National Institutes of Natural Sciences*
[3]*Institute for Integrated Radiation and Nuclear Science, Kyoto University*
[4]*National Institutes for Quantum and Radiological Science and Technology*
[5]*Institut Laue-Langevin*

INTRODUCTION: The molecular machinery of the cyanobacterial circadian clock comprises three proteins: KaiA, KaiB, and KaiC. Through interactions among the three Kai proteins, the phosphorylation states of KaiC generate circadian oscillations *in vitro* in the presence of adenosine triphosphate (ATP). In this system, KaiA, KaiB and KaiC periodically assemble into a large complex, which is considered to play the key role of the negative feedback loop of circadian rhythm. Recently, the cryo-electron microscopy (EM) structure of the ABC complex has been reported. However, the N-domains of KaiA subunits were poorly resolved due to their missing electron density maps. The whole structure of ABC complex has remained to be elucidated. Herein, for characterization of the overall structure of ABC complex, we conducted integrative techniques using small-angle X-ray scattering (SAXS), inverse contrast-matching small-angle neutron scattering (iCM-SANS) in conjunction with computer simulations.

EXPERIMENTS: X-rays from a high-brilliance point-focused X-ray generator (MicroMAX-007HF, Rigaku, Tokyo, Japan) were focused with a confocal mirror (OptiSAXS) and collimated with a confocal multilayer mirror and two pinholes collimation system with the lower parasitic scattering, "ClearPinhole". The scattered X-rays were detected with a two-dimensional semiconductor detector (HyPix-6000, Rigaku, Tokyo, Japan). The sample-to-detector distance and wavelength of X-ray used for present work was 1320 mm and 1.542 Å, respectively. For removal of unfavorable aggregates from the sample solution, the laboratory-based SEC-SAXS System (LA-SSS) was employed to measure the SAXS profile in the Q range (0.01 $Å^{-1}$–0.2A^{-1}). The SANS experiments were performed using the D22 instrument installed at the Institut Laue-Langevin (ILL), Grenoble, France. The sample-to-detector distance and wavelength of neutron used for present work was 5600 mm and 6.0 Å, respectively. SEC-SANS system was also utilized for present work.

RESULTS:
Small-angle X-ray and inverse contrast matching small-angle neutron scatterings coupled with size-exclusion chromatography provided constraints to highlight the spatial arrangements of the N-terminal domains of KaiA, which were not resolved in the previous structural analyses. We computationally built 3D models of the overall structure of ABC complex, which reproduced the SAXS and iCM-SANS profiles. Computationally built 20 million structural models of the complex were screened out utilizing the constrains resulting from scattering data and then subjected to molecular dynamics simulations to examine their stabilities. Our modeling procedure is described Fig.1.

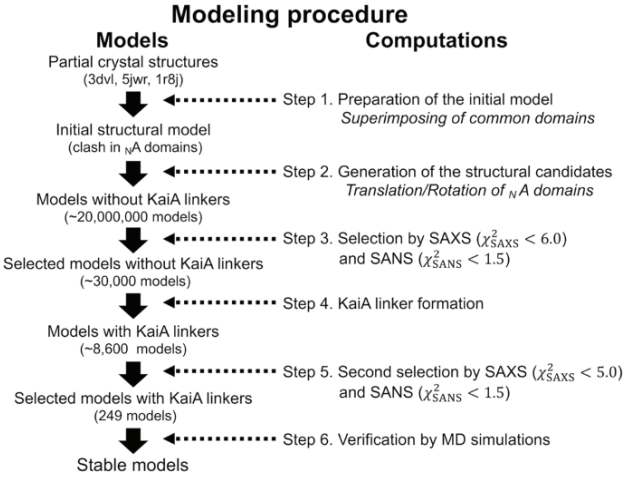

Fig. 1. Modeling procedure of the overall structure of ABC complex.

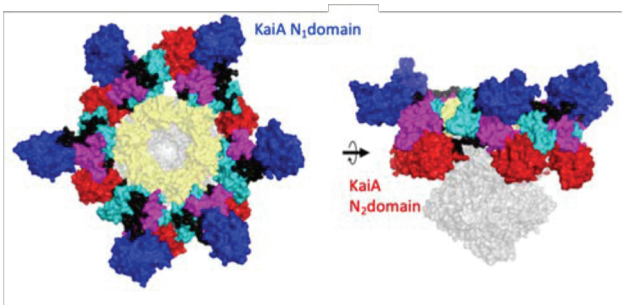

Fig. 2. Top and side view of the ABC complex structure after 100 ns MD simulation

The final model (Fig.2) suggests that, despite large fluctuation of the KaiA N-terminal domains, their preferential positionings mask the hydrophobic surface of the KaiA C-terminal domains, hindering additional KaiA-KaiC interactions.
Thus, our integrative approach provides a useful tool to resolve large complex structures harboring dynamically fluctuating domains.

REFERENCES:
[1] M. Sugiyama *et al.*, Sci. Rep., **6:35567** | (2016).
[2] Y. Yunoki *et al.*, Commun. Bio., **5:184** | (2022).

CO6-15 Analysis of p53 aggregates for elucidation of aggregation mechanism

E. Hibino, K. Morishima[1], R. Inoue[1], M. Sugiyama[1] and H. Hiroaki.

Graduate School of Pharmaceutical Science, Nagoya University
[1]Institute for Integrated Radiation and Nuclear Science, Kyoto University

INTRODUCTION: The tumor suppressor protein p53 is a transcription factor that induces DNA repair proteins when DNA is damaged or induces apoptosis when DNA damage is severe, thereby preventing cells from turning cancerous. In fact, p53 mutations are found in half of all cancers, and preservation of p53 function is important in terms of cancer prevention. However, the development of therapeutic drugs targeting p53 has been challenging. It has been reported that the DNA-binding domain of p53 is aggregation-prone, that the introduction of hot spot mutations common in cancer increases its aggregation, and that the aggregates that form are heterogeneous [1,2].

We recently found that the environments in which amyloid aggregates and amorphous aggregates of p53C tend to form are distinct. They found that high salt and sugar concentrations inhibited amorphous aggregate formation of p53C and suppressed loss of function [3]. However, the mechanisms of p53 aggregation nucleation and elongation remain unresolved, which has been an obstacle in the development of p53-related cancer drugs. The objective of this study is to elucidate the mechanism of aggregation.

EXPERIMENTS: The p53-DNA binding domain (p53C) protein was produced as a GST-fused form in an E. coli expression system. After GST tag affinity purification, the GST tag was cleaved with HRV3C protease and finally purified by size exclusion chromatography. The protein solution was aggregated with the addition of Reagent A, and then sonicated for DLS measurement.

DLS measured by using a system equipped with a 22-mW He-Ne laser, an Avalanche Photo Diode mounted on static/dynamic compact goniometer, ALV/LSE-5003 electronics, and ALV-5000 Correlator. Incident angles were 45°, 60°, 75°, 90°, 105°, 120°, and 135°, and measurements were taken three times at each angle.

RESULTS: We have previously found that p53C becomes predominantly amyloid aggregates when Reagent A is added. p53C aggregate is very difficult to analyze because it is formed as a mixture of amorphous and amyloid aggregates under normal conditions. Thus, we decided to characterize the amyloid aggregates by comparing them without and with Reagent A. Amorphous and amyloid aggregates were sonicated and observed under a microscope, and many small granular aggregates were observed. The granular aggregates were measured by DLS and found to be a mixture of several sizes of aggregates (Fig. 1). Similar profiles were obtained for the amorphous and amyloid aggregates, but the results suggest that the amyloid aggregate exhibits periodicity. Further analysis is needed to characterize specific amyloid aggregates exclusively.

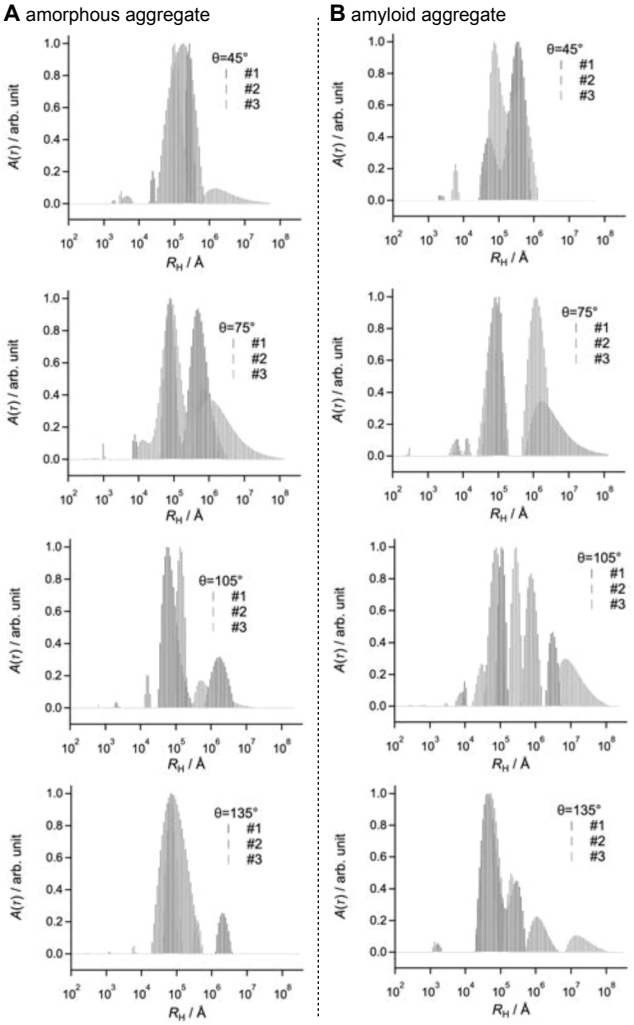

Fig. 1 Overlay of the DLS results of 3 measurements at each angle for amorphous aggregates (**A**) and amyloid aggregates (**B**).

REFERENCES:

[1] A.P.D.A Bom, L.P. Rangel, D.C.F.Costa, G.A.P. de Oliveira, D. Sanches, C.A. Braga, L.M. Gava, C.H.I. Ramos, A.O.T. Cepeda, A.C. Stumbo, C.V.D.M. Gallo, Y. Cordeiro and J.L. Silva, J. Biol. Chem., **287** (2012) 28152-18162.

[2] S. Ghosh, S. Salot, S. Sengupta, A. Navalkar, D. Ghosh, R. Jacob, S.D.R. Kumar, N.N.J.S. Sahay, S. Mehra, G.M. Mohite, S.K. Ghosh, M. Kombrabail, G. Krishnamoorthy, P. Chaudhari and S.K. Maji, Cell Death Differ. **24** (2017) 1784-1798.

[3] E. Hibino, T. Tenno and H. Hiroaki, Biophys. Rev., **14** (2022) 267-275.

CO6-16 Development of hydroponics system for wheat cultivation

N. Sato, R. Urade, A. Okuda, K. Morishima, R. Inoue, and M. Sugiyama

Institute for Integrated Radiation and Nuclear Science, Kyoto University

INTRODUCTION: Wheat flour has been widely served as staple foods in many countries. In most cases, wheat flour is mixed with salts and water and kneaded to produce wheat dough, which is then processed to make various wheat food products: bread, noodles and cookies. The quality of those foods such as the rise of the bread and firm chewiness is much affected by the physical properties of wheat dough. It is well-known that gluten is a key component for determining the physical properties of wheat dough. Gluten is a composite of two major wheat proteins, glutenin and gliadin. Glutenin is high-molecular-weight network polymer protein, which is responsible for elasticity of dough. Gliadin, in contrast, is an aggregated monomeric protein, which is responsible for viscosity of dough. Thus gluten inherits both properties of those two proteins, but it is possible that the composite formation of two proteins brings new properties unique to gluten. Therefore nanoscale structural analysis of the wheat proteins is necessary to make clear how glutenin and gliadin behave in the molecular scale and how they interact in the gluten. However, structural analysis of food materials often becomes a difficult work because they are generally opaque, condensed, disordered, and multicomponent systems. Small-angle scattering technique is one of effective method to overcome this difficulty. It has been utilized for a variety of soft matters including rubber, gels, colloids, and other condensed materials. From this viewpoint, we have been applying small-angle technique to the structural analysis of wheat proteins. In our recent study [1], aqueous solutions and hydrated solids of gliadins have been investigated by small-angle X-ray scattering (SAXS). As a result of this study, we demonstrated that gliadin monomers dispersed isolatedly in low-concentration aqueous solutions, but with increasing concentrations they gradually associate together to form multimolecular domains with interparticle interference. It was also revealed that at much higher concentrations gliadins become insoluble in water to form hydrated aggregates with density fluctuation inside and the correlation length of this fluctuation becomes smaller with increasing gliadin concentrations. To understand the structure of gluten, however, it is insufficient to clarify the structure of gliadin or glutenin alone because gluten consists of a composite of gliadin and glutenin. Several schematic illustrations have been presented so far, the detail of molecular scale structure of gluten is still unknown. We accordingly employ small-angle neutron scattering (SANS) with contrast variation technique to address this problem. Unlike X-ray scattering, neutrons are scattered by nuclei of atoms, and the scattering power depends on isotopes. Deuterium and hydrogen have different neutron scattering power. Therefore a part of multicomponent systems are deuterated, it has different contrast compared with the non-deuterated parts. If this fact is applied to the structural analysis of gluten, the structure of gliadin alone is observed in the gluten composite by mixing deuterated gliadin and mixed with non-deuterated glutenin. The largest difficulty of this concept lies on the difficulty of sample preparation. The deuterated proteins are often expressed in *E. coli* grown in heavy water and deuterated carbon sources. However recombinant wheat proteins have not yet been successfully obtained. Thus we planned to grow wheat by hydroponics using heavy water to prepare deuterated gliadin. As a first step, we built a hydroponics system optimized for the cultivation of wheat. Here we report the details of these system.

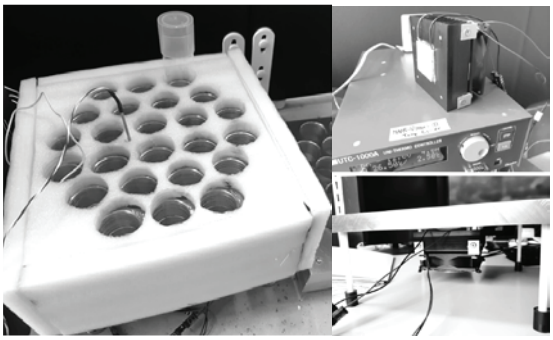

Fig. 1 The hydroponics system for wheat cultivation. (Left) Temperature-controlled container for cultivation vials. (Right top) Peltier device, heatsink, cooling fan and Peltier controller. (Right bottom) Peltier cooling unit installed under the container base.

DESIGN AND FABRICATION: Hydroponics of wheat is planned to conduct by the method reported by Singh and Jenner [2]. First, wheat seeds are grown in planter soil placed in a growth chamber. After the ears emerge, stems are cut and put into water in the cultivation vials. These vials are maintained at 1–2°C until the ears ripens. To keep low temperature, a temperature-controlled vial container with Peltier-cooling system was developed. A Peltier device (TEC1-12706) attached to an aluminum heat sink (30×98×100 mm) and DC fan (92×92×25 mm, 1400 rpm) was driven by a Peltier controller (UTC-1000A, Ampere inc.). A 24-hole vial container made of an aluminum block was manufactured in the factory of KURNS and temperature probe of Peltier controller was inserted into the container.

RESULTS: When the container holding 24 vials filled with 100mL of water was cooled placed in a chamber at 20°C, the container was successfully kept at 1°C for more than two weeks. This result shows that this system can be safely used for hydroponics of wheat.

REFERENCES:

[1] N. Sato *et al.*, *J. Agric. Food Chem.*, **63** (2015) 8715–8721.

[2] B. K. Singh and C. F. Jenner, *Aust. J. Plant Physiol.*, **10** (1983) 227–236.

CO6-17 Preparation and Characterization of BPA-uridine conjugate for BNCT

K. Tanabe[1], M. Suzuki[2], and T. Nishihara[1]

[1]*Department of Chemistry and Biological Science, College of Science and Engineering, Aoyama Gakuin University*

[2]*Institute for Integrated Radiation and Nuclear Science, Kyoto University*

INTRODUCTION:

Modified nucleobases are widely used as antitumor agents, and a variety of them have important functions in vivo. Among them, 5-fluorouridine (5FU), 5-fluorodeoxyuridine (FdUrd), and cytarabine are well-known antitumor agents, and their modified derivatives are utilized as stimuli-responsive prodrugs.[1]

Recently, we employed uridine with three alcohol units as a solubilizer for poorly soluble compounds and prepared BPA-uridine conjugates for boron neutron capture therapy (BNCT). We found that irradiation in the presence of BPA-uridine markedly enhanced the cytotoxicity of the radiation. In this study, we conducted a in vivo study of BPA-uridine conjugate. Eventually, we confirmed that BPA-uridine showed robust cytotoxic effect on tumor tissue upon thermal neutron irradiation. Thus, uridine seems to be good agents for drug delivery system.

EXPERIMENTS:

Preparation of BPA-uridine conjugate. BPA was added to the aqueous solution of uridine under basic conditions to solubilize the conjugate. After the BPA was dissolved in the aqueous solution, the resulting solution was neu-tralized and then subjected to in vivo experiments. **Neutron capture therapy to A549 tumor models.** A549 cells in matrigel (1×10^6 cells per mouse) were subcuta-neously inoculated into the right thighs of BALB/c nude mice. The tumors were allowed to grow ~1.5 month. The mouse was injected with fructose-BPA or uridine-BPA (250 mg/kg). The mice were placed in acrylic which were secured on a 5-mm-thick thermoplastic plate that con-tained 40 weight % (wt %) of ^{6}LiF (96% 6Li) to block thermal neutrons and had a circular hole in the center. The thigh containing the tumor was stretched over the hole, and the tumor was irradiated with epi-/thermal neu-trons for 50 min, 1 h after the injection. The tumor size was measured by a caliper, and tumor volume (V) was calculated using the following equation: $V = ab^2/2$, where a and b are the major and minor axes, respectively.

RESULTS:

Conventionally, fluctose has been used to solubilize BPA in water for the formation of their complex that showed hydrophilic properties. We expected that the uridine bearing ribose unit formed similar complex with BPA, and thus we combined BPA with uridine and prepared their conjugate. Eventually, we found that BPA-uridine conjugate was smoothly dissolved in water, and then applied them to cellular experiments.

In the research process to date, fructose has been used to solubilize BPA in water to form a complex that exhibits hydrophilic properties. Therefore, we expected that uridine, which has a ribose unit, would form a similar complex with BPA. Last year, we synthesized the BPA-uridine complex and confirmed that it dissolves smoothly in water. We also applied the complex to cell experiments and found that it exhibited high cytotoxicity under thermal neutron irradiation.

To determine whether the BPA-uridine conjugate is effective in vivo, we administered this conjugate to BALB/cAJcl nude mice with A549 tumors. We administered this conjugate to BALB/cAJcl nude mice with A549 tumors to characterize its efficacy in vivo. A549 cells were transplanted into BALB/cAJcl nude mice (n = 3 per group) and allowed to grow until the tumor size was about 100 mm^3. The conjugate was then administered subcutaneously and changes in tumor size after thermal-neutron irradiation were recorded.

As shown in Figure 1B, the BPA-uridine conjugate efficiently inhibited tumor growth at the same level as BPA-fluctose. These results suggest that BPA-uridine was activated within the tumor upon irradiation conditions and exhibited a cell-killing effect even in vivo.

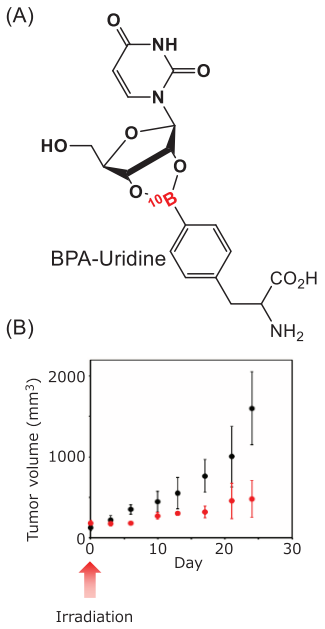

Figure 1. (A) Chemical structure of BPA-Uridine conjugate (B) In vivo evaluation of BPA-uridine as an anticancer agent. Tumor volumes of each group (BPA-uridine (+: red, -: black), epi-/thermal neutrons: 50 min.

REFERENCES:

[1] K. Tanabe *et al.*, *Org. Biomol. Chem.* **7** (2009), 651–654.

CO6-18 Analysis of distinct amyloid formation pathways between bovine and human insulin

K. Yuzu, T. Nozaki, K. Morishima[1], A. Okuda[1], R. Inoue[1], M. Sugiyama[1], E. Chatani

Graduate School of Science, Kobe University

[1]Institute for Integrated Radiation and Nuclear Science, Kyoto University

INTRODUCTION: Amyloid fibrils are a form of protein aggregates that are associated with various amyloidoses and neurodegenerative diseases. The formation of amyloid fibrils is typically progressed through nucleation and growth phases. The nucleation phase is a rate-limiting step, and once amyloid nuclei are formed, the subsequent rapid elongation of amyloid fibrils is induced. However, much remains unclear about the aggregation mechanisms during the nucleation phase.

In this study, we investigated the fibrillation process of bovine and human insulin, the amino acid sequences of which are slightly different. We previously identified that bovine insulin formed prefibrillar intermediates in early stage of the fibrillation [1, 2]. Here, we performed small-angle X-ray scattering (SAXS) and analytical ultracentrifugation (AUC) measurements to identify and compare the fibrillation process of two species of insulin.

EXPERIMENTS: A sample of 5.0 mg/mL bovine and human insulin dissolved in 25 mM HCl containing 0.1 or 0.5 M NaCl was heated at 75 °C. At different time points, the reaction was instantly stopped with cooling on ice and the samples were subjected to subsequent measurements.

The SAXS profile was collected at 25 °C with a NANOPIX equipped with a HyPix-6000 (Rigaku Corporation, Japan). A Cu K-α line (MicroMAX-007HFMR) was used as a beam source, which was further focused and collimated with a confocal multilayer mirror (OptiSAXS). The camera length was set to 1.33 nm and the range of the scattering vector q was from 0.005 to 0.20 Å^{-1}.

AUC was conducted with a ProteomeLab XL-I analytical ultracentrifuge (Beckman Coulter, USA). Sedimentation velocity analytical ultracentrifugation (SV-AUC) measurements were performed using Rayleigh interference optics at 40,000 rpm at 20 °C with a 1.5 mm path-length cell. The experimental data were analyzed with SEDFIT software. The density and viscosity of solvent, and partial specific volume of each protein were calculated from their amino acid sequences with SEDNTERP software.

RESULTS: We first performed SAXS measurements to investigate the amyloid formation process of bovine and human insulin (Fig. 1). In both insulin species, the SAXS profiles at 60 min, when the fibrillation was completed, showed the higher scattering intensity especially in lower q region compared to those before the reaction, indicating the fibrillation was successfully observed by SAXS measurements. The slope of the log-log plot at 60 min was close to -1, which is consistent with the rod-like morphology of amyloid fibrils. Interestingly, the SAXS profile of bovine insulin at 10 min exhibited a scattering pattern intermediate between those before the reaction and at 60 min. These observations indicate the formation of prefibrillar intermediates in the process of amyloid formation of bovine insulin in accordance with our previous observation [2]. On the other hand, the SAXS profile of human insulin at 10 min showed almost the same pattern as that before the reaction, suggesting the absence of prefibrillar intermediates in the fibrillation process of human insulin.

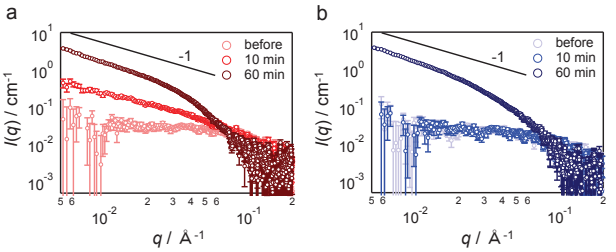

Fig. 1. SAXS profiles of bovine (a) and human insulin (b). The insulin samples heated in the presence of 0.1 M NaCl were subjected to the SAXS measurements.

We further performed SV-AUC measurements to examine the early aggregation process of two species of insulin (Fig. 2). The sedimentation coefficient distribution of bovine insulin showed rapid evolution of aggregates, while those of human insulin showed no significant aggregation. These results indicate that bovine insulin forms oligomers leading to the formation of prefibrillar intermediates immediately after the initiation of the reaction, unlike typical amyloid formation pathway with a lag phase observed in human insulin.

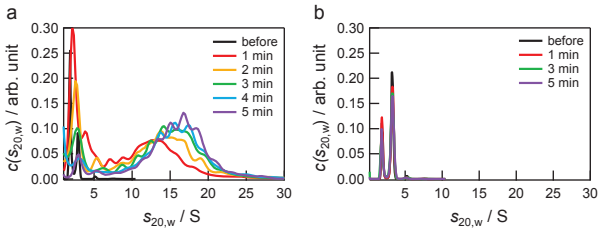

Fig. 2. Sedimentation coefficient distribution of bovine (a) and human insulin (b). The insulin samples heated in the presence of 0.5 M NaCl were subjected to the AUC measurements. For bovine insulin, sample solutions were diluted 2-fold with 25 mM HCl before measurement to suppress flocculation of aggregates induced by cooling.

REFERENCES:

[1] E. Chatani *et al.*, *J. Biol. Chem.*, **289** (2014) 10399-10410.

[2] E. Chatani *et al.*, *Sci. Rep.*, **5** (2015) 15485.

CO6-19 Structural analysis of protein complex using analytical ultracentrifugation and small-angle X-ray scattering.

K. Morishima[1], A. Okuda[1], M. Shimizu[1], N. Sato[1], R. Inoue[1], M. Sugiyama[1]

[1]*Institute for Integrated Radiation and Nuclear Science, Kyoto University*

INTRODUCTION:

Structural analysis of a protein complex in solution is essential to understanding physiological phenomena in biological systems. Small-angle X-ray scattering (SAXS) is powerful technique which gives three-dimensional structure of a biomacromolecule in solution. To obtain the high-quality structural model, it is crucial to obtain an scattering profile purely corresponding to the target protein complex. On the other hand, because protein complexes and dissociated proteins coexist in the solution under dissociation-aggregation equilibrium, the experimental scattering profile is offered as an ensemble-average of them. Therefore, it is necessary to extract the scattering profile of the concerned protein complex from the ensemble-averaged profile.

Recently, size-exclusion chromatography (SEC)-SAXS attracts an attention to obtain the scattering profile of the concerned component in a multi-component solution. However, SEC-SAXS is unavailable for a weakly-bound complex because they break down in the SEC process.

In this study, we developed the integrated analytical method with analytical ultracentrifugation (AUC) and SAXS, AUC-SAXS, to derive the scattering profile of a weakly-bound complex under dissociation-aggregation equilibrium [1].

EXPERIMENTS:

AUC-SAS was demonstrated for the following two systems:

(i) The complex of the ubiquitin-like domain of the proteasome shuttle factor hHR23b and PUB domain of N-glycanase: The sedimentation equilibrium (SE)-AUC and SAXS was conducted for the mixture (hHR23b + PUB) with equimolar ratio (100 μM + 100 μM and 50 μM + 50 μM).

(ii) The complex of clock protein KaiA and KaiC: The sedimentation velosity (SV)-AUC and SAXS was conducted for the mixture (KaiA + KaiC) with the ratio of 2 : 6 (5.7 μM + 17 μM).

SAXS measurements were carried out with NANOPIX (Rigaku). AUC measurements were conducted with a ProteomeLab XL-I (Beckman Coulter). All measurements were conduceted at 25 ºC

RESULTS:

Considering the equilibrium to be A + B ↔ AB for proteins A, B, and complex AB, the scattering profile of the solution under dissociation-aggregation equilibrium is expressed as

$$I(q) = c_{\mathrm{A}} i_{\mathrm{A}}(q) + c_{\mathrm{R}} i_{\mathrm{R}}(q) + c_{\mathrm{AR}} i_{\mathrm{AR}}(q) \quad (1)$$

Here, q and $I(q)$ are the magnitude of scattering vector and experimentally obtained scattering intensity, respectively. c_j and $i_j(q)$ are the concentration of component j and scattering intensity per the concentration of component j. In AUC-SAXS, in order to derive the scattering profile of the complex $i_{\mathrm{AB}}(q)$, $I(q)$, $i_{\mathrm{A}}(q)$, and $i_{\mathrm{B}}(q)$ are individually measured with SAXS, and c_js for all components are obtained with AUC.

For the system of hHR23b + PUB, c_js for all components were calculated with the dissociation constant K_{D}, which was obtained with SE-AUC. Closed circles in Figure 1 show the scattering profile for the complex of hHR23b and PUB $i_{\mathrm{AB}}(q)$. The obtained $i_{\mathrm{AB}}(q)$ was not explained by the simple docking model between hHR23b and PUB (gray line in Figure 1). Then, we performed a normal mode analysis using the docking model as an initial structure. Finally, the optimal three-dimensional structure model that reproduces $i_{\mathrm{AB}}(q)$ was offered (black line and inset in Figure 1).

With the same procedure, the scattering profile of the complex of KaiA and KaiC was obtained. The three-dimensional structure model that reproduces the scattering profile was revealed with the molecular dynamics simulation.

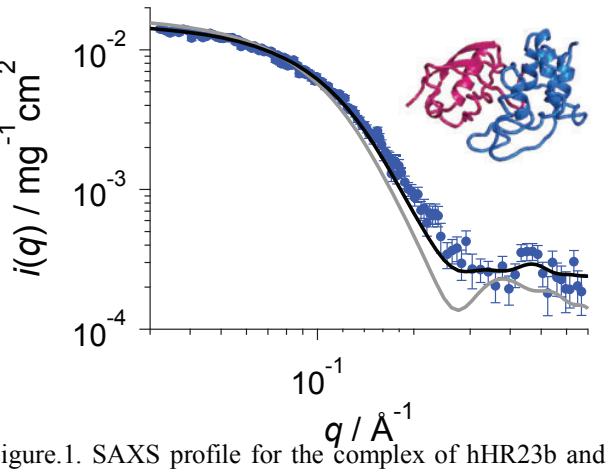

Figure.1. SAXS profile for the complex of hHR23b and PUB $i_{\mathrm{AB}}(q)$ (closed circles). Gray and black lines are the profiles calculated from the docking simulation model and the optimized model (inset) with the normal mode analysis.

REFERENCES:

[1] K. Morishima, *et al*. *Commun. Biol.* **3**, 294 (2020).

CO6-20 Dynamics of copper chaperone for superoxide dismutase studied by small-angle X-ray scattering

M. Shimizu[1], R. Inoue[1], Y. Furukawa[2], A. Okuda[1], K. Morishima[1], N. Sato[1], R. Urade[1], and M. Sugiyama[1]

[1]*Institute for Integrated Radiation and Nuclear Science, Kyoto University*
[2]*Department of Chemistry, Keio University*

INTRODUCTION: Many proteins are composed of multiple structural domains, and function by dynamically changing their domain arrangement. X-ray solution scattering measurement is a useful research technique for structural analysis of such dynamic biomolecules; All molecules with various structures contribute to the scattering data. We have attempted to analyze molecular structures of a multi-domain protein ER-60 based on small-angle X-ray scattering (SAXS) profiles [1].
Here, we focused on a multi-domain protein copper chaperone for superoxide dismutases (CCS) and study its behavior in solution. This protein passes Cu ion to Cu, Zn superoxide dismutases (SOD1), probably via flexible domain dynamics [2]. CCS monomer has three functional domains, and domain II of CCS bind to each other to form CCS homodimer [3]. We studied structure of the CCS dimer in solution by small angle X-ray scattering. In this study, a mutant CCS, which is more likely to maintain its dimeric state than wildtype CCS, was chosen for measurement.

EXPERIMENTS: A mutant human CCS protein was expressed using *Escherichia coli* and purified. Small-angle X-ray scattering (SAXS) was measured by a NANOPIX (Rigaku, Tokyo, Japan). From the raw scattering data, one dimensional SAXS profile was calculated using SAngler [4]. Oligomeric state of CCS in sample solution was examined by analytical ultracentrifugation. The analytical ultracentrifugation was conducted with a ProteomeLab XL-I analytical-ultracentrifuge (Beckman Coulter). The content of each oligomer was calculated using SEDFIT [5]. Both the Small-angle X-ray scattering experiment and analytical ultracentrifugation were performed at 25ºC. Scattering profile of dimeric CCS was calculated by combining the SAXS profile and analytical ultracentrifuge data, following a previous report [6]. SAXS profiles of atomistic models were calculated with Pepsi-SAXS [7].

RESULTS: We measured scattering profile of apo-state of the mutant CCS. The profile changed gradually with time; an increase in the radius of gyration of the sample was observed over time. This can be interpreted as the formation of CCS aggregates composed of non-native structure of CCS, which are caused by the radicals produced upon X-ray irradiation. For wild type CCS, it has already been reported that components other than dimeric CCS can contribute significantly to the SAXS profile [8]. Although we utilized a mutant CCS that could potentially suppress the formation of multimers larger than dimers, the SAXS measurements did not show the expected results. Therefore, we considered the data from the first 10 minutes of the measurement as the SAXS profile of the aggregate-free CCS.
Abundance of each CCS multimer was measured using analytical ultracentrifugation, and SAXS profile of the CCS dimer was calculated using the data.
Subsequently, we examined whether the SAXS profile matched already studied tertiary structures. Currently, a structure of the CCS dimer can be modeled using known crystal structures of CCS [3, 9]. In addition, A theoretical predicted structure of the CCS by AlphaFold are also available [10, 11]. We generated one CCS dimer model from crystal structures, and generated one CCS dimer model from the AlphaFold model. The predicted SAXS profiles of these structures were different from our experimental profile; χ^2 values were 7.71 and 7.39, respectively. This result suggests that the structure of CCS dimer in solution is different from its crystal structure.
Further improvement of the measurement conditions, such as the addition of radical scavengers to the sample buffer, is expected to enable the acquisition of more accurate scattering curves.

REFERENCES:
[1] A. Okuda *et al.*, *Sci. Rep.*, **11** (2021) 5655.
[2] P. J. Schmidt *et al*., *J. Biol. Chem.*, **275** (2000) 33771-33776.
[3] A. L. Lamb *et al*., *Biochemistry*, **39** (2000) 1589-1595.
[4] N. Shimizu *et al.*, *AIP conf. Proc.*, **1741** (2016) 50017.
[5] M. Sawicki, *Publ. Astron. Soc. Pac.*, **124** (2012) 1208-1218.
[6] K. Morishima, *Commun. Biol.*, **3** (2020) 294.
[7] S. Grudinin *et al*., *Acta Cryst.*, **D73** (2017) 449-464.
[8] G. S. A. Wright *et al*., *Biochem. J.*, **439** (2011) 39-44.
[9] F. A. Sala *et al*., *PLos Biol.*, **17** (2019) e3000141.
[10] J. Jumper *et al*, *Nature*, **596** (2021) 583-589.
[11] M. Varadi *et al*, *Nucleic Acids Research*, **D1** (2021) D439-D444.

CO6-21 Structural dynamics of the overlapping di-nucleosome

H. Tanaka[1], M. Nishimura[1, 2], K. Nozawa[1], K. Morishima[3], R. Inoue[3], H. Ehara[4], S. Sekine[4], M. Sugiyama[3], and H. Kurumizaka[1, 2]

[1]Laboratory of Chromatin Structure and Function, Institute for Quantitative Biosciences (IQB), The University of Tokyo
[2]Department of Biological Sciences, School of Science, The University of Tokyo
[3]Institute for Integrated Radiation and Nuclear Science (KURNS), Kyoto University
[4]RIKEN Center for Biosystems Dynamics Research

INTRODUCTION:
In eukaryotes, the genomic DNA is hierarchically folded as chromatin. The basic repeating unit of chromatin is termed nucleosome, in which approximately 145 base pairs of DNA wrap around an octameric histone core containing two copies of each core histone, H2A, H2B, H3, and H4. In the process of chromatin remodeling, a collision of two adjacent nucleosomes can form an alternative structural unit such as overlapping dinucleosome: OLDN [1]. We have previously reported that the crystal structure of the OLDN, in which the octameric histone core, and the hexameric histone core lacking one copy of H2A-H2B dimer, are tightly associated with each other, and 250 base pairs of DNA are continuously wrapped around it [2]. Subsequent molecular dynamics simulations, small-angle x-ray, and neutron scattering (SAXS and SANS, respectively) analysis suggested that the OLDN adopt a variety of conformations in solution [3]. Here, we combined cryo-electron microscopy (cryo-EM) and analytical ultracentrifuge (AUC) with SAXS to characterize the structural dynamics of the OLDN.

EXPERIMENTS:
The OLDN sample was prepared by the salt dialysis method and purified by nondenaturing gel electrophoresis as previously described [2]. For cryo-EM analysis, OLDN was fixed by the glutaraldehyde crosslinking through the gradient fixation method. The micrographs were acquired using a cryo-EM: Tecnai Arctica transmission electron microscope (FEI), equipped with a K2 summit direct electron detector (Gatan). Single-particle analysis of the OLDN was performed on RELION 3.1 software. SAXS analysis was performed with a NANOPIX instrument (RIGAKU) at the Institute of Radiation and Nuclear Science, Kyoto University. To cover the wide q-range, we employed two sample-to-detector distances: 1,330 mm and 350 mm and combined these data. We performed the standard procedures of transmission correction, buffer solution scattering subtraction, and conversion to an absolute scale with water scattering. We also performed AUC to correct the SAXS data by removing the SAXS profile portion derived from slight aggregates as previously described [4].

RESULTS:
We collected 1737 k particle images from 2833 of micrographs and then removed junk particles throughout the following 2D and 3D classification. Using the 1330 k particles, we performed a 3D classification of OLDN. Consequently, 12 OLDN structures, that exhibit different orientations of the octasome unit and the hexasome unit were observed. We built structural models from four of these classes and determined cryo-EM structures of OLDNs. We then performed AUC-SAS to obtain the refined SAXS profile of the OLDN and plotted the calculated SAXS curves of the four cryo-EM structures with it. Notably, the theoretical SAXS curve derived from the open OLDN configuration fitted to the experimental SAXS curve with the reconstituted OLDN. This result suggests that the various relative orientations between the two histone cores, octasome and hexasome, observed in cryo-EM experiments reflect the structural dynamics of the OLDN in solution.

REFERENCES:
[1] M. Engeholm *et al.*, Nat Struct Mol Biol. **16** (2009) 151-158.
[2] D. Kato *et al*., Science. **356** (2017) 205-208.
[3] A. Matsumoto *et al*., Biophys J. **118** (2020) 2209-2219
[4] K. Morishima *et al*., Commun. Biol. **3** (2020) **294**.

R3079

CO6-22 ^{11}C medical-isotope production via the ^{12}C(γ,n)^{11}C reaction with carbon nano tube

N. Takahashi[1,2], Y. Kosuge[1,2], M. Kurosawa[1], M. Tamura[1], M. Fujiwara[1,2], T. Kubota[3], N. Abe[4], and T. Takahashi[4]

[1]*Research Center for Nuclear Physics, Osaka University*
[2]*Kyoto Medical Technology*
[3]*Agency for Health, Safety and Environment, Kyoto University*
[4]*Institute for Integrated Radiation and Nuclear Science, Kyoto University*

INTRODUCTION: L-[^{11}C]-Methionine is used as a positron emission tomography (PET) reagent for medical diagnosis of brain tumors [1]. The medical ^{11}C radioisotopes are mostly produced in a cyclotron via the ^{14}N(p,α)^{11}C reaction by bombarding enriched nitrogen gas with a proton beam [2]. In Japan, Hokkaido University and Osaka University have worked in collaboration with Sumitomo Heavy Industries to obtain the government permission for the PET examination with L-[^{11}C]-Methionine for checking the metastasis and recurrence test of the brain tumor patient [3,4].

Instead of producing ^{11}C with the cyclotron, we tried a novel method of producing ^{11}C using the bremsstrahlung γ-rays with a carbon nano tube (CNT) target to get a reasonable number of the ^{11}C specific activity.

Fig. 1 shows a schematic illustration to produce ^{11}C isotopes from a CNT target and to extract them as $^{11}CO_2$ gas.

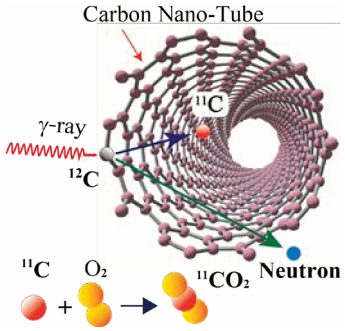

Fig. 1. Scheme of the ^{11}C medical-isotope production via the ^{12}C(γ,n)^{11}C reaction with a CNT target. Neutron and ^{11}C are released from the strong bonding network of CNT after the ^{12}C(γ,n)^{11}C reaction following the nuclear two-body kinematics. Since the recoiled ^{11}C is chemically active, a $^{11}CO_2$ molecule is produced via the $^{11}C+O_2 \rightarrow {}^{11}CO_2$ chemical process.

EXPERIMENTS: We prepare the O_2 gas circulation system, consisting mainly of 1) a CNT target with a nanotube powder, 2) O_2 gas tubes, and 3) molecular sieves. We seal the CNT powders in the Al target vessel with non-woven masks as gas inlet/outlet filter. We trap the $^{11}CO_2$ using the molecular sieves. The ^{12}C(γ,n)^{11}C reaction experiment has been done using the bremsstrahlung γ-rays generated with a 40 MeV electron beam at the electron LINAC facility.

Fig. 2 shows the experimental scheme to measure the $^{11}CO_2$ yields from the ^{12}C(γ,n)^{11}C reaction. The $^{11}CO_2$ gas flows out from the CNT target and is trapped in two molecular sieve capsules. The radioactive ^{11}C with a half-life of 20 minutes emits a positron. 511-keV γ-rays from positron-electron annihilation are detected using the CdZnTe detectors. Taking into account the incompleteness of trapping $^{11}CO_2$ gas with molecular sieves, we prepared two molecular sieve capsules to correct for the trapping efficiency.

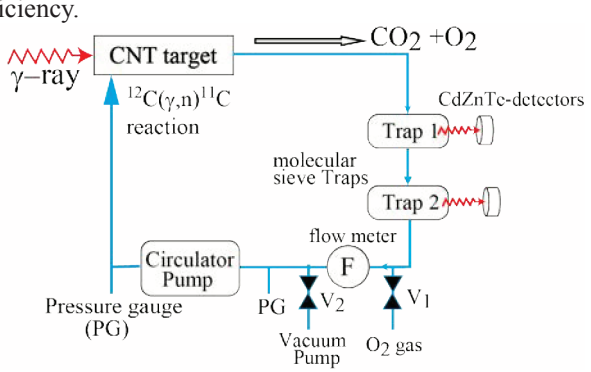

Fig. 2. Experimental scheme to measure the $^{11}CO_2$ extraction rate.

We confirmed that the $^{11}CO_2$ flowed out from the CNT target capsules by observing 511-keV γ-rays from $^{11}CO_2$ trapped in the molecular sieves. The measured decay curve obtained by measuring 511 keV γ-rays as a function of elapsed time was well in agreement with the ^{11}C half-life of 20 minutes. Several forms such as multiwall CNT, single-wall CNT, C60, and graphene were examined to achieve high yields of $^{11}CO_2$.

RESULTS: We conclude that the extraction rate of $^{11}CO_2$ from the single-wall CNT target can be as high as 15%. With this extraction rate of 15%, we estimate that we can obtain the ^{11}C activity of 34 GBq when we use a single-wall CNT target under the conditions with 1) a length of 50 cm, 2) weight of 1.13 kg for 0.155 g/cm^3, 3) a 40 MeV electron beam intensity of 100 μA for 40 minute bombardment. This 34 GBq radioactivity is enough amounts for one patient's diagnosis. The detailed report will be published in the near future [5].

REFERENCES:

[1] Y. Komatsu *et al.*, Radioisotopes, **67** (2018) 75.
[2] T.J. Ruth. A.P. Wolf, IEEE Trans., NS-**26** (1979) 1710.
[3] M. Kinoshita *et al.*, J. Neurosurg **125** (2016) 1136.
[4] M. Kameyama *et al.*, Eur. J. Nucl. Med. Mol. Imaging **43** (2016) 2267.
[5] M. Kurosawa *et al.*, to be published.

CO6-23 Distribution of the chemical modifications of the amino acid residues in lens structural proteins during development of age-related cataract

S. Matsushita[1], Y. Suzuki[1], A. Nakamura[1] and T. Takata[2]

[1] *Dept of Materials and Applied Chemistry, Nihon University*
[2] *Institute for Integrated Radiation and Nuclear Science, Kyoto University*

INTRODUCTION:
Imaging mass spectrometry (Imaging MS) is a technique to visualize the localization of a target peptide by scanning mass spectrometry on tissue and superimposing positional information [1]. The method is based on the conventional mass spectrometers, thus depending on the fragmentation of each peptide.

Continuing from the previous year, we tackled to screen the best fragmentation pattern for visualizing the localization of chemical modifications that accumulate in lens structural protein with aging. Now, target modification is the isomerization of Aspartate residues (iso-Asp). Protein-constituting Asp isomerizes spontaneously with aging (four types iso-Asp series: L-α-Asp, L-β-Asp, D-α-Asp, and D-β-Asp) and accumulates with aging [2]. Therefore, identification of iso-Asp is a useful predictor as a new definition of aging.

In previous year, we found out the isomerization of Asp151 in αA-crystallin in the soluble fraction of porcine lens. This Asp is the homologous position of Asp151 in those of human lens αA-crystallin, which was heavily isomerized. We chemically synthesized this target peptide, including Asp151, and a fragmentation pattern was decided using by quadrupole type mass spectrometer. At the next step, we attempted to make a frozen section of the porcine lens on a prep for imaging MS. However, it was technically difficult to prepare the frozen section of lens due to the rich water molecules and high concentrated protein in lens. Therefore, we changed the target peptide in mouse lens, which is easier to handle, and resumed studies.

EXPERIMENTS:
Material Mouse lens was homogenized and fractionated by centrifugation to isolate lens water soluble (WS) fractions. The WS proteins were dissolved and applied for trypsin digestion as previously reported [2]. The peptide, corresponding of the mouse αA-crystallin 169–180 (^{169}VQSGLDAGHSER^{180}), was synthesized by Fmoc-based solid-phase peptide synthesis (PSSM-8; Shimadzu). The crude peptides were purified by reverse-phase HPLC using a C18 column (Capcell Pak C18; Shiseido) as previously reported [3].
LC-MS analysis Asp-containing peptides were detected by the multiple reaction monitoring (MRM) method using a triple quadrupole mass spectrometer (LCMS-8060; Shimadzu). Briefly, solutions containing 0.1–1 μg of peptides was applied into LCMS-8060, then fragmentation pattern was optimized. Then, the HPLC separation for tryptic peptide of mouse lens WS was carried out (Nexera X2, Shimadzu) using a combination of a C18 column (L-column2 ODS, CERI). The binary mobile phase compositions were 0.1% formic acid/water (mobile phase A) and 0.1% formic acid/acetonitrile (mobile phase B). The linear gradient was 0–45% phase B for 60 min at a flow rate of 0.2 mL/min, and a column temperature of 35°C.

RESULTS:
Prior to analysis, survey for the valid MRM transitions of target peptides of mouse αA-crystallin 169–180 was performed. The MRM method for Asp-containing peptide was created with Lab Solutions software (Shimadzu, Japan). The MRM chromatograms for fragment ions of target peptide was acquired with the transitions as shown in Table 1.

	sequence	MRM transitions for mouse peptide
human	^{146}IQTGL**D**ATHAER^{157}	1254.30 > 1236.25
pig	^{146}VPSGV**D**AGHSER^{157}	CE: 51.0
mouse	^{169}VQSGL**D**AGHSER^{180}	Positive ion mode

Table. 1. αA-Crystallin derived peptide sequence and MRM transition for mouse peptide

Next, the isomerization of Asp174 of mouse αA-crystallin was investigated (Fig. 1). AS shown in Fig. 1, we were able to confirm five peaks including the four iso-Asp residues. One more peak may be a peak derived from isomerization of other amino acids, such as Glutamate residue at 179. That result implied the usefulness determination of fragmentation pattern of this peptide was successful. It may still present problem to digest lens tissue on plate, but we could apply this method for frozen section of the mouse lens for imaging MS.

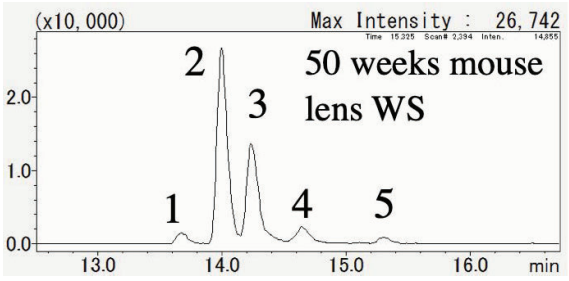

Fig. 1. LC-MS-MRM chromatogram of Asp174 peptide isomers of αA-crystallin in the water soluble fraction derived from the lens of a mouse.

REFERENCES:
[1] M. Stoeckli *et al.*, Nat. Med., **7** (2001) 493-496.
[2] N. Fujii *et al.*, J. Biol Chem., **287** (2012) 663-669.
[3] K. Magami *et al.*, PLoS One., **16** (2021) 0250277.

CO6-24 Molecular dynamics analysis of oxidative folding enzyme ER-60 with solution scattering measurement

A. Okuda, M. Shimizu, K. Morishima, Y. Yunoki, R. Inoue, N. Sato, R. Urade and M. Sugiyama

Institute for Integrated Radiation and Nuclear Science, Kyoto University

INTRODUCTION: ER-60, an oxidative protein folding enzyme that belongs to the PDI family, is a multi-domain protein consisting of four thioredoxin-like domains, **a** and **a'** domains with catalytically active cysteine pairs and chaperone association **b** and **b'** domains in the order **a-b-b-b'-a'**. The oxidized form of active cysteine pairs (ox) catalyses the oxidation reaction of dithiol on an unfolded protein, while the reduced form (red) catalyses the reduction or isomerization of disulphide bonds. In this process, ER-60 might have the appropriate domain conformations and arrangement in order to function, and it is estimated that the structure fluctuates and changes according to the redox state of active cysteine pairs in the solution [1]. Inverse Contrast Matching Small-Angle Neutron Scattering (iCM-SANS) [2], which takes advantage of the large difference in neutron scattering length between hydrogen and deuterium, is useful for observing the dynamics and structures of such multi-domain proteins in solution.

When hydrogenated and 75% deuterated proteins are in 100% deuterated solvent, the deuterated proteins become scatteringly invisible, and only the scattering of the specific part that is hydrogenated could be observed. Applying this method to multi-domain proteins, the domain motion of the hydrogenated domains could be selectively observed. To achieve this method for multi-domain proteins, the hydrogenated and deuterated domains must be prepared separately and then connected by protein ligation technique.

To reveal the structure-function correlations of ER-60, we aim to analyze selective domain dynamics by iCM-SANS. For this purpose, we connected the hydrogenated and deuterated domains with the ligation enzyme, *Oa*AEP.

EXPERIMENTS: Because 75% deuterated recombinant protein requires *E. coli* to be cultured in 75% deuterated M9 medium [3], we examined culture conditions in M9 medium and M9 plus medium [4] in addition to LB broth. Each recombinant protein containing 75% deuterated protein (**a** domain) was purified using a His-tag affinity column and a ion-exchange column. The deuteration rate of 75% deuterated protein was calculated by mass spectrometry with MALDI-TOF MS using a previously reported [3]. The 75% deuterated **a** domain and the hydrogenated **bb'a'** domain were mixed in buffer containing 200 mM Tris-HCl (pH 7.4) / 150 mM NaCl. Then, 0.2 μM of the ligation enzyme *Oa*AEP was added to the mixture, and the protein ligation reaction was performed at 20°C for 64 hours. The results of ligation reactions were confirmed by SDS-PAGE.

RESULTS: **a** domain was more abundant in the M9 medium, so we proceeded to perform 75% deuteration in this medium. In Fig. 1A, expression and purification of the recombinant 75% deuterated **a** domain yielded a highly purified protein sample. The deuteration rate of 75% deuterated **a** domain was calculated to be 73.6% from the increase in mass due to deuteration of un-exchangeable hydrogen obtained from MALDI-TOF MS (Fig. 1B).

The results of the protein ligation reaction are shown in Fig. 2. The band of ligation product, **a-bb'a'**, connecting **a** and **bb'a'** domains was observed, indicating the progress of the protein ligation reaction. Currently, we are investigating conditions to increase the efficiency of the ligation reaction for iCM-SANS, are also carrying out ligation reactions at other ligation sites, and are planning to measure the preliminary structure of them by SAXS.

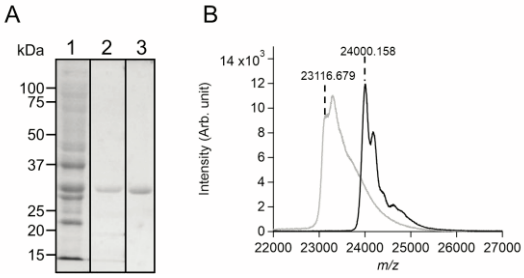

Fig. 1. (A) Expression and purification of recombinant 75% deuterated **a** domain of ER-60. Recombinant a domain of ER-60 expressed in E. coli in 75% D_2O M9 medium (lane 1) were purified by His-tag column chromatography (lane 2) and ion-exchange chromatography (3). Proteins in each effluent were separated by SDS-PAGE and stained with CBB. (B) Mass spectra of hydrogenated (gray line) and 75% deuterated (black line) **a** domain of ER-60.

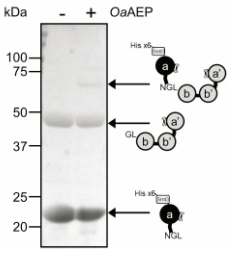

Fig. 2. The ligation product from 75% deuterated **a** domain and hydrogenated **bb'a'** domain of ER-60 by *Oa*AEP (reaction times of 64 h at 20°C). Proteins were separated by SDS-PAGE and stained with CBB.

REFERENCES:

[1] M. Sugiyama *et al.*, J. Appl. Crystallogr., **47** (2014) 430–435.
[2] A. Okuda *et al.*, Sci Rep., **11** (2021) 5655.
[3] A. Okuda *et al.*, Biophys Physicobiol., **18** (2021) 16-27.
[4] M. Cai *et al.*, J Biomol NMR., **66** (2016) 85-91.

CO6-25 Integrative approach using SAXS / SANS and computational science for understanding the structure-function relationship of IDP

T. Oda, R. Oi[1], R. Inoue[2], K. Morishima[2], H. Nakagawa[3], T. Tominaga[4], M. Sugiyama[2], and M. Sato[1]

Department of Life science, Rikkyo University
[1]Graduate school of Medical Life science, Yokohama City University
[2]Institute for Integrated Radiation and Nuclear Science, Kyoto University
[3]Materials Sciences Research Center, Japan Atomic Energy Agency
[4]Neutron Science and Technology Center, Comprehensive Research Organization for Science and Society (CROSS)

INTRODUCTION: Intrinsically disordered proteins (IDP), which do not have a rigid folded structure, play important roles in living cells. However, due to its flexibility, it is difficult to understand its function based on its structure. Small-angle X-ray scattering (SAXS) is a useful method to analyze IDP because it provides dynamic structural information of IDP in an aqueous solution. We analyzed a protein Hef involved in the repair of DNA damage. Hef consists of two folded domains (Helicase domain and Nuclease domain), which are connected by an intrinsically disordered region (IDR) [1]. Based on SAXS data, we analyzed the dynamic structure of Hef as an ensemble of computationally generated structures. The ensemble showed that the structure of Hef is slightly more compact rather than that expected to be a random structure, suggesting a relationship with its function. However, in SAXS, the scattering from the two domains and the IDR are all observed as one scattering curve, therefore the interpretation of the ensemble analysis remains arbitrary. When we preparer segmentally deuterated Hef and measure small-angle neutron scattering (SANS), we can obtain structural information of selected region from hydrogenated one utilizing inverse contrast matching SANS (iCM-SANS) [2]. In this study, we prepared segmentally deuterated Hef and checked degree of deuteration and structural integrity. This integrative approach is expected to play a significant role for the analysis of IDP.

EXPERIMENTS:
Preparation of segmentally deuterated Hef- In a conventional contrast matching method, SANS of protein is measured in 40% (v/v) D_2O solvent. In this condition, hydrogenated protein is matched out, and scattering of 100% deuterated protein can be observed. However, under this condition, incoherent scattering from 60% (v/v) H_2O becomes large noise. On the other hand, if we prepare a 75% deuterated protein and measured in a 100% D_2O solvent, the 75% deuterated protein will be matched out and scattering of only the hydrogenated protein can be observed [2]. Under this condition, incoherent scattering from solvent is significantly lower than 40% D_2O. Therefore, in this study, the deuteration degree was set to ~75%. We prepared two segmentally deuterated Hef. One is (75D)Helicase/(H)IDR-(H)Nuclease and the other is (H)Helicase-(H)IDR/(75D)Nuclease. The (75D)Helicase and the (75D)Nuclease were expressed in *Escherichia coli* cells which is cultured in M9 medium containing 75% (v/v) D_2O, 1.5 g/L of D-body glucose and 0.5 g/L of H-body glucose. After extraction from the cells and purification, the 75D-proteins were ligated to the hydrogenated proteins using a protein ligation enzyme NpuDnaE.
Determination of the degree of deuteration of proteins- The degree of deuteration of proteins were determined using a MALDI-TOF MS. From the peak shift value between ($\Delta m/z$) the 75D- and the H-protein, degree of deuteration was calculated by the following formula [3]; degree of deuteration (%) = $((\Delta m/z)/N)*100$, where N corresponds to a total number of non-exchangeable hydrogen of a protein.
SAXS measurement of segmentally deuterated Hef- The SAXS measurements of segmentally deuterated Hef were performed using a KUR SAXS instrument. Prior to SAXS measurement, samples were dialyzed against 100% D_2O solvent, and the protein concentration was adjusted to 0.8 mg/mL.

RESULTS: We succeeded in preparation of segmentally deuterated Hef. Milligram order of segmentally deuterated Hef, which is enough to use SANS measurement, was obtained. Although the degrees of deuteration of the Helicase and the Nuclease were expected to be 75%, it must be confirmed. Actual degrees of deuteration of the Helicase domain and the Nuclease domain were 79.6% and 70.0% respectively. This information is crucial for fulfilling the precise contrast matching of solvent to the prepared protein and estimate of residual scattering of deuterated region. Prior to SANS analysis, we performed SAXS analysis to check structural integrity of segmentally deuterated Hef in 100% D_2O solvent. The R_g values of (79.6D)Helicase/(H)IDR-(H)Nuclease and (H)Helicase-(H)IDR/(70.0D)Nuclease were 50±2Å and 48±1Å respectively. These values are slightly larger than that of non-deuterated Hef in 100% H_2O solvent (45±1Å). This indicates that these segmentally deuterated Hef contain a small amount of aggregation. Stress during dialysis to the 100% D_2O solvent or transport of sample may have caused sample aggregation. To obtain fine data in SANS, we further have to optimize preparation and transport of sample.

REFERENCES:
[1] Ishino *et al.,* J. Biol. Chem. 289;31, 21627-21639 (2014).
[2] Sugiyama *et al.,* J. Appl. Cryst. 47, 430–435 (2014).
[3] Okuda *et al.,* Biophys Physicobiol 6;18, 16-27 (2021).

CO6-26 Development of New Treatment Method for Epithelioid Sarcoma by BNCT

T. Fujimoto[1, 2], T. Andoh[3], Y. Sakurai[4], M. Suzuki[4]

[1]*Department of Orthopaedic Surgery, Hyogo Cancer Center*
[2]*Department of Orthopaedic Surgery, Kobe University Graduate School of Medicine*
[3]*Faculty of Pharmaceutical Sciences, Kobe Gakuin University*
[4]*Institute for Integrated Radiation and Nuclear Science, Kyoto University*

INTRODUCTION: Epithelioid sarcoma (ES) is an extremely rare malignant soft tissue tumor that predominates in young adults [1]. Because it is not sensitive to anticancer drugs and radiation therapy, wide surgical excision is the basis of treatment. On the other hand, good therapeutic effects of boron neutron capture therapy (BNCT) on soft tissue sarcoma have been reported [2, 3]. Therefore, in this study, BNCT was performed on ES-bearing animals at the Institute for Integrated Radiation and Nuclear Science, Kyoto University (KURNS), and its antitumor effect was examined.

EXPERIMENTS: Using nude mice, a cancer-bearing animal model was prepared by transplanting a human-derived ES cell line (VA-ES-BJ) [4] into the subcutaneous space of the mouse right thigh. After the tumor grew, tumor volume was calculated from the tumor diameter. Then animals were divided into 3 groups (n=4) of A, B, and C, and the A and B groups were used as controls. In group C (BNCT), 45 minutes after intravenous administration of BPA (500 mg/kg), and in group B without administration of BPA, only the right lower limbs of both groups were irradiated with epithermal neutrons for 10 minutes. The tumor volume of the entire group was measured from the day of irradiation (day 0), and 14 days after irradiation, the tumor tissue was removed and histological examination was performed immediately after expiry.

RESULTS: Fourteen days after irradiation, tumor regression was observed only in group C. Histological examination revealed apoptotic tumor cells in the fibrotic tissue in group C [Fig. 1], while tumor cells in the other groups were still growing [Fig. 2]. The equivalent dose of group C obtained from the dose measurement was 8.7 Gy-Eq for the skin and 20.7 Gy-Eq for the tumor, indicating a selective dose for the tumor.

DISCUSSION: In recent years, it has been suggested that epigenetic-related enzyme EZH2 target inhibitors may improve the therapeutic outcome of advanced ES [5]. Furthermore, here, for the first time, it was clear that ES regressed with only one irradiation by BNCT in this study. Therefore, a new treatment method is expected to be developed in future that combines systemic treatment with drug therapy, local treatment surgery and local treatment with BNCT.

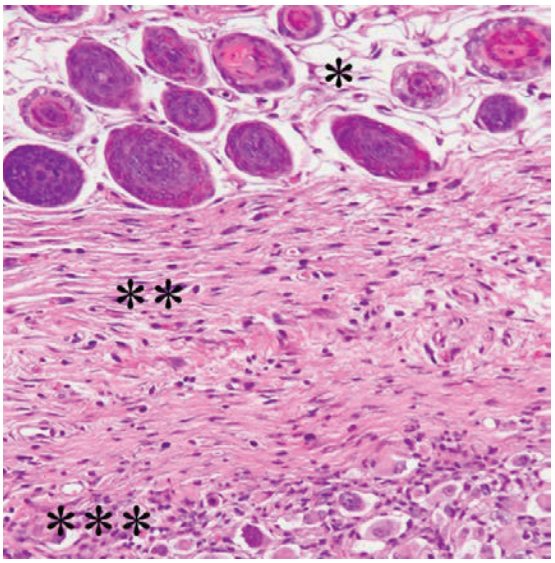

Fig. 1. Histopathological study (HE staining) of group C (BNCT) reveals apoptotic tumor cells (***) are gradually replaced with connective tissue (**). No damage to normal cells was observed on skin or subcutaneous area (*) by BNCT.

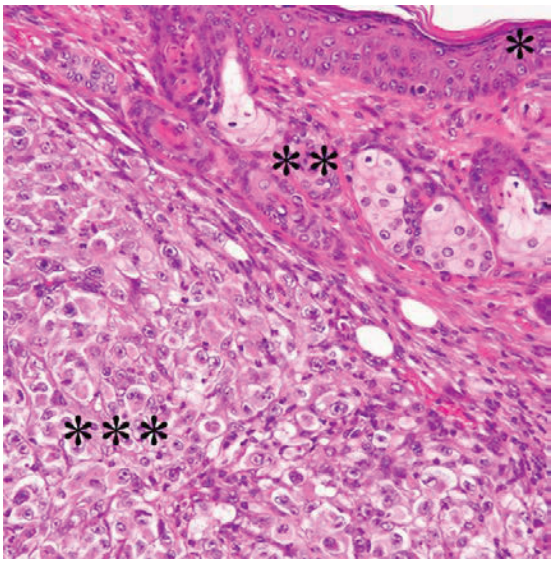

Fig. 2. Histopathological study (HE staining) of group B (hot control) reveals no tumor cells (***) are destroyed, and no normal cells (*, **) are damaged. *, skin; **, subcutaneous space.

REFERENCES:

[1] AM. Frezza *et al.*, JAMA Oncol., **4** (2018):e180219. doi:10.1001/jamaoncol.2018.0219.
[2] T. Fujimoto *et al.*, Appl Radiat Isot., **166** (2020). doi: 10.1016/j.apradiso.2020.109324.
[3] T. Fujimoto *et al.*, Appl Radiat Isot., **169** (2021). doi: 10.1016/j.apradiso.2020.109407.
[4] C. Helson *et al.*, Int J Oncol. **7** (1995). doi: 10.3892/ijo.7.1.51.
[5] M. Gounder *et al.*, Lancet Oncol. **21** (2020). doi: 10.1016/S1470-2045(20)30451-4.

CO6-27 Elucidating the Molecular Basis for the Increased Risk of Nuclear Cataract Development with Global Warming

T. Takata[1] and N. Yamamoto[2]

[1] *Institute for Integrated Radiation and Nuclear Science, Kyoto University*
[2] *Research Promotion Headquarters, Fujita Health University*

INTRODUCTION:
The transparency of the lens is important for focusing target onto retina. Maintaining the function of lens determines the quality of life. Lens cells contain rich structural proteins, which is called as crystallin. Those stable long-lived crystallin interactions is critical for lens functions. Many past studies have reported about post-translational modifications in crystallin species decreased solubility of crystallins and lead senile cataract formation in aged lens. Those modifications were accumulated under various stresses during life, such as heat and ultraviolet (UV) irradiation. It has also been considered that many factors in addition to UV are the main causes of nuclear cataract (NUC). In order to elucidate those factors, we performed a worldwide epidemiological survey and confirmed that the risk of NUC is significantly higher in residents living in areas where the annual number of days with temperatures of 30°C or higher is higher. Furthermore, in an *in silico* simulation study, the applicant group showed that the incidence of NUC differs within a range of internal temperature differences (35.0-37.5°C). These obvious but new results are currently the focus of worldwide attention. Based on these results, this study aims to clarify the relationship between NUC and environmental temperature. We cultured lens model cells in different temperature and analyzed the modification levels of Aspartate (Asp) in crystallin to verify the mechanism of NUC onset in different temperature.

EXPERIMENTS:
Material Immortalized human lens epithelial cells (iHLEC-NY2) are cultured on different temperature (35.0-37.5°C) and collected by RIPA buffer or PBS. Cell pellets was solubilized by sonication, 6 M Guanidine hydrochloric acid, 8 M Urea or MPEX solution (GL Science). All denaturants were removed by reverse phase spin column, then used for trypsin digestion.
LC-MS analysis After trypsin digestion, each tryptic peptide was injected to LC-MS/MS systems to identify the expressed αA-crystallin in iHLEC-NY2. Each sample was eluted over 60 min with a linear gradient (5%–45%) formed by mixing solvent A (0.1% formic acid aqueous solution) and solvent B (100% acetonitrile containing 0.1% formic acid). The algorism for the database search was Proteome Discoverer 1.0 (ThermoFisher) as previously reported [1].
D/L analysis Next, the same sample was applied into LC-Q-MS/MS systems to evaluate isomerization levels of Asp58 in αA-crystallin. The mass chromatogram was depicted as previously reported [2].
Western Blotting In order to get intense peptides chromatograms from isolated αA-crystallin, on membrane digestion was considered. To get unique αA-crystallin band on PVDF membrane, electrophoresis for cell extracts and immunoblotting for αA-crystallin was performed with a monoclonal antibody against human αA-crystallin (Santa).

RESULTS:
In the preliminary study phase, the tryptic digestion for the cell extracted by RIPA buffer did not show the chromatograms. Based on the possibility that tryptic digestion was not possible due to the surfactant in RIPA buffer used for collecting cells, we used PBS for collecting cells. We next solubilized cell extracts using by denaturants (guanidine hydrochloric acid or urea). Solubilized samples were diluted for trypsin digestion followed by LC-MS/MS analysis, but no peak was observed. Considering the possibility that denaturants inhibited trypsin digestion, we changed denaturant into to the MPEX solution systems. All preparation included a desalting step before tryptic digestion. While the identification of human αA-crystallin in iHLEC-NY2 was successful, the quantitatively analysis of Asp58 in αA-crystallin was not. The peak on chromatogram was very poor, and not enough to evaluate the peak areas (Fig. 1). Though the molecular weight is specified, there are numerous peaks, although originally four peaks should have been seen even if isomerization was included. It is possible that background is seen due to the low total intensity.

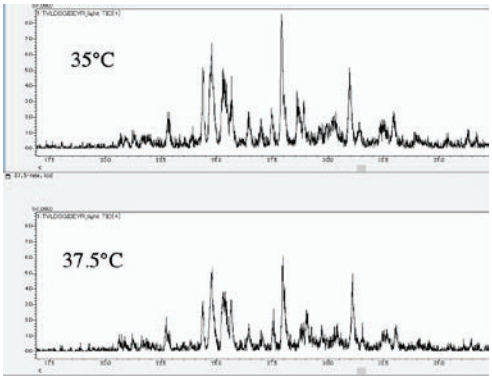

Fig. 1. Modifications on Asp151 of αA-crystallin in iHLEC extracts.

Western blot analysis showed a 20 kDa protein in iHLEC cells, that was strongly immunoreactive with the anti-αA-crystallin antibody (data not shown). The on membrane digestion for quantitative analysis should be in future study.

REFERENCES:
[1] N. Fujii *et al.*, J. Biol Chem., **287** (2012) 663-669.
[2] N. Fujii *et al.*, ACS Omega., **5** (2020) 27626-27632.

CO6-28 IL-6 suppresses the increase in cell oxidation through phosphorylation of mTOR and is involved in the acquisition of radiation resistance of the human pancreatic cancer-derived cell line Panc-1.

Y. Tamari[1,2], G. Kashino[3], M. Suzuki[2]

[1]*Department of Radiology, Kyoto Prefectural University of Medicine*
[2]*Institute for Integrated Radiation and Nuclear Science, Kyoto University*
[3]*RI center, Nara Medical University*

INTRODUCTION: Interleukin 6 (IL-6) is a multifunctional cytokine. The detailed mechanism of radiation resistance acquisition by IL-6 has not been elucidated. Our previous studies have revealed that the acquisition of radiation resistance by IL-6 is caused by suppressing mitochondrial-derived oxidative stress after γ-ray irradiation [1]. mTOR exists as a regulator of various phenomena such as cell metabolism, growth, proliferation and survival. It has been reported that mTOR is regulated by the IL-6 signaling pathway [2]. Furthermore, suppression of active oxygen by mTOR has been reported [3], and it was hypothesized that mTOR is involved in the radiation resistance acquisition mechanism through suppression of intracellular oxidation degree by IL-6. Purpose of this study is to investigate the detailed mechanism of radiation resistance acquisition through suppression of oxidative stress by IL-6.

EXPERIMENTS: The human pancreatic cancer derived cell line Panc-1 was used. Recombinant IL-6 (rIL-6) was administered 24 hours prior to 4 Gy X-ray irradiation or analysis. The ELISA method was used to examine the amount of IL-6 produced by Panc-1. In addition, a colony formation assay was performed to investigate the acquisition of radiation resistance by IL-6. Furthermore, the protein expression level downstream of IL-6 was confirmed by Western blotting. At that time, rapamycin was used to investigate the involvement of mTOR in the IL-6 signaling pathway. Fluorescent probes Mitosox Red and JC-1 were treated and fluorescence intensities were measured to measure mitochondrial superoxide levels and membrane potentials, respectively.

RESULTS: As a result of ELISA, Panc-1 produced considerably less IL-6. However, the survival rate after X-ray irradiation was significantly increased when rIL-6 was administered. Activation of STAT3 was shown when rIL-6 was administered, which was suppressed by administration of the mTOR inhibitor rapamycin. The acquisition of radiation resistance by IL-6 in Panc-1 and the involvement of mTOR located downstream of IL-6 were clarified. The amount of active oxygen in mitochondria was increased by X-ray irradiation, but was suppressed by administration of rIL-6. However, administration of rapamycin neutralized the effects of IL-6. On the other hand, the decrease in mitochondrial membrane potential due to X-ray irradiation was suppressed by rIL-6. Regarding the mitochondrial membrane potential, the effect of IL-6 was canceled by suppressing mTOR.

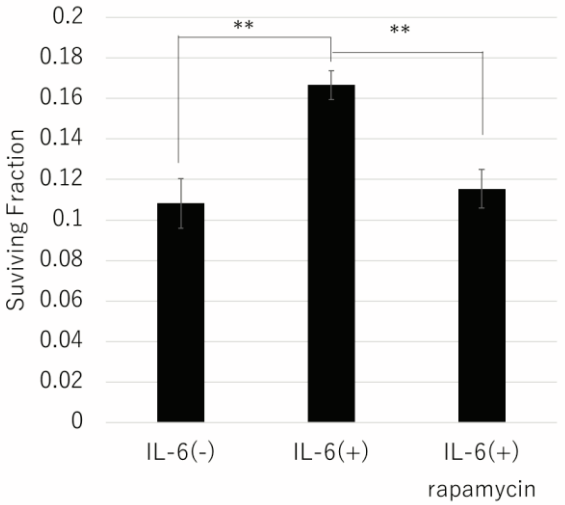

Fig. 1. Effect of mTOR inhibition on radiation resistance acquisition. Mean±SD result are graphed (**p<0.001)

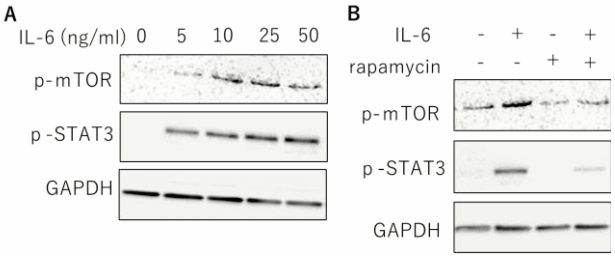

Fig.2. Activation of mTOR and STAT3 by IL-6. (A) Phosphorylation of mTOR and STAT3 depending on the concentration of rIL-6 was observed. (B) Phosphorylation od mTOR and STAT3 was suppressed by rapamycin.

REFERENCES:

[1] Y. Tamari *et al*., J. Radiat. Res., **58** (2017)412-420.
[2] JH. Kim *et al.*, J. Biol. Chem., **283** (2008)708-715.
[3] J. Hu *et al*., Int. J. Biochem. Cell Biol., **89** (2017) 42-56.

CO6-29 Production of medical radioisotopes using electron linear accelerator

S. Sekimoto, M. Inagaki and T. Ohtsuki

Institute for Integrated Radiation and Nuclear Science, Kyoto University

INTRODUCTION: A shortage in the supply of ^{99}Mo resulting from the shutdown of reactors used for its production is a global problem. Because ^{99}Mo is an indispensable source of ^{99m}Tc, which is used in nuclear medicine to make diagnoses using techniques such as scintigraphy and single photon emission computed tomography (SPECT), a stable supply of ^{99}Mo is vital. Therefore, production of ^{99}Mo by using neutrons or protons generated in accelerators has been investigated [1–3]. To separate ^{99m}Tc from ^{99}Mo produced by an accelerator, methods based on sublimation, solvent extraction, and ion-exchange column chromatography have been examined and developed [2,4–6]. In addition, Gopalakrishna et al. have reported the preparation of ^{99}Mo by the ^{100}Mo(γ,n) reaction using bremsstrahlung photons [6], followed by conventional solvent extraction using methyl ethyl ketone (MEK) and zirconium (Zr) molybdate gel to separate ^{99m}Tc. According to the regulations of the Japanese pharmacopeia, the extraction using organic materials and the gel method using heavy metal elements such as Zr are not approved for the ^{99m}Tc-separation methods. Additionally, it is also difficult and impractical to use the sublimation method, which requires complicated and/or large scale devices for the mass-production of pure ^{99m}Tc. Recently, Kaken Inc. developed a new method, known as the "technetium master milker" (TcMM). This technique can produce highly pure ^{99m}Tc at a maximum activity of 1.85×10^{13} Bq (500 Ci) per batch from ^{99}Mo of low specific activity [7]. We carried out the production of ^{99}Mo by the ^{100}Mo(γ,n) reaction using bremsstrahlung photons generated in an electron linear accelerator (LINAC), a technique that has not been investigated significantly in Japan. The amounts of ^{99}Mo produced at several electron energies (E_e) were examined. To separate ^{99m}Tc from the irradiated target, in this work, the TcMM was applied to the ^{99}Mo produced by LINAC, and the subsequent yield of ^{99m}Tc was evaluated.

RESULTS: An example of the specifications for a LINAC necessary for the production of a stable supply of ^{99}Mo is now discussed. As mentioned by Gopalakrishna et al. [6], an expansion of ^{99}Mo production to clinical levels requires the scaling up of the specifications for the LINAC, such as E_e, beam current of electrons, amount of target material, irradiation time, and so on. Additionally, to reduce target material costs, the use of $^{nat}MoO_3$ is preferable to that of $^{100}MoO_3$. If $^{nat}MoO_3$ is used as the target instead of $^{100}MoO_3$, the amount of the target material must be increased by one order of magnitude. Therefore, this increase in the quantity of target material necessitates a new system designed to irradiate the bulky target with bremsstrahlung photons effectively.

Here, we show the specification for LINACs where the target ($^{100}MoO_3$), mean current, and operation time are 10 g, 100 μA, and 20 h, respectively, and E_e is varied from 21 to 41 MeV. The ^{99}Mo activity produced at each E_e and its dependence on operation time and elapsed time are shown in Fig. 1. To efficiently produce ^{99}Mo and reduce the production of radioactive impurities, the E_e must be optimized. Based on the experimental results in this work, the optimized E_e is 35 MeV (see Fig. 1). Therefore, if the LINAC were operated at E_e of 35 MeV, 44.0 GBq of ^{99}Mo would be produced, and if subsequent purification of ^{99m}Tc by TcMM were carried out more than three times, about 100 GBq of ^{99m}Tc would be obtained a few days after source irradiation. Because the required activity of ^{99m}Tc in Japan is about 1000 GBq per day, 30 LINACs with the specifications would be able to supply the Japan's demand for ^{99m}Tc in a few days.

The specifications of the LINAC are general and practical. Furthermore, because LINACs can be downsized, it is possible to set up compact LINACs for the production of ^{99}Mo-^{99m}Tc in different locations in Japan and even around the world. In the near future, the installation of a new complex using the LINAC ^{99}Mo-production system and ^{99m}Tc-separation system by the TcMM would be desirable. Such complexes must be compact and inexpensive to allow their installation at many clinics and hospitals.

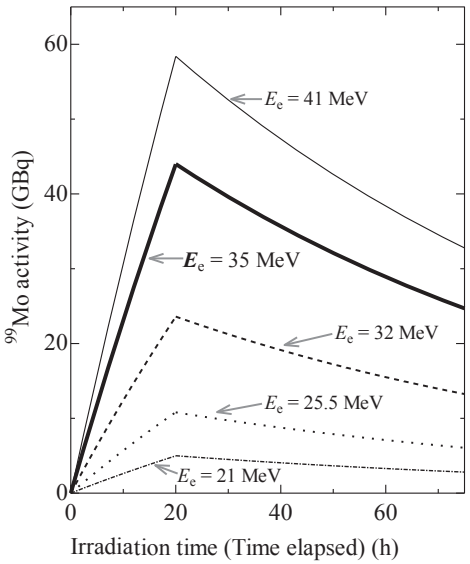

Fig. 1. Estimation of ^{99}Mo-activity based on the LINAC's specification.

REFERENCES:

[1] Y. Nagai *et al.*, J. Phys. Soc. Jpn., **82** (2013) 064201.
[2] Y. Nagai *et al.*, J. Phys. Soc. Jpn., **83** (2014) 083201.
[3] K. Nakai *et al.*, Proc. Jpn. Acad. Ser. **B 90** (2014) 413–421.
[4] M. Kawabata *et al.*, J. Phys. Soc. Jpn., **84** (2015) 023201.
[5] K. Mang'era *et al.*, J. Radioanal. Nucl. Chem., **305** (2015) 79-85.
[6] A. Gopalakrishna *et al.*, J. Radioanal. Nucl. Chem., **308** (2016) 431-438.
[7] K. Tatenuma *et al.*, Radioisotopes **63** (2014) 501-513.

CO6-30 Design, Synthesis, and Evaluation of Polyamine-type Boron & Gadlinium Carriers for NCT

S. Aoki[1,2], H. Ueda[1], M. Suzuki[3], T. Tanaka,[1] S. Masunaga[3], N. Kondo[3], and Y. Sakurai[3]

[1]*Faculty of Pharmaceutical Sciences, Tokyo University of Science*
[2]*Research Institute for Science and Technology, Tokyo University of Science*
[3]*Institute for Integrated Radiation and Nuclear Science, Kyoto University*

INTRODUCTION: Neutron capture therapy using boron-10 (^{10}B) (BNCT) is one of powerful therapies for local tumor control in the treatment of brain tumor, melanoma, and related diseases [1].

We previously reported on the design and synthesis of phenylboronic acid pendant-cyclen (cyclen = 1,4,7,10-tetraazacyclododecane) [2]. Based on its high intracellular uptake in cancer cell, we designed and synthesized several phenylboronic acid-pendant 9-, 12-, and 15-membered macrocyclic amines such as **^{10}B-1a~3a** and their corresponding Zn^{2+} complexes **^{10}B-1b~3b** (Fig. 1) [3]. The experimental results suggest that the metal-free **^{10}B-1a~3a** are introduced into cancer cells (A549 and HeLa S3 cells) more efficiently than their Zn^{2+} complexes **^{10}B-1b~3b** into normal cells with considerably high cancer/normal cells selectivity. Besides, it was found that 12- and 15-membered derivatives **^{10}B-2a~3a** exhibit a higher BNCT effect than 9-membered **^{10}B-1a**, possibly because **^{10}B-2a~3a** form the corresponding Zn^{2+} complexes **^{10}B-2b~3b**, which strongly interact with DNA double strand in living cells, resulting in the efficient breakdown of DNA double-strand upon the neutron irradiation.

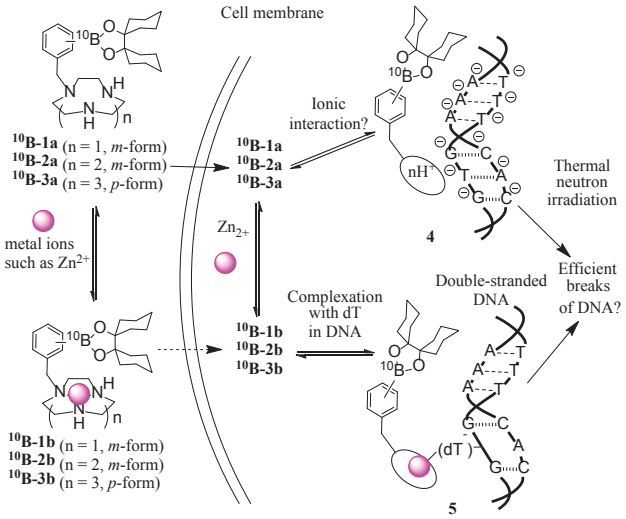

Fig. 1. Structures of boron-containing macrocyclic polyamines and the corresponding Zn^{2+} complexes and the proposed scheme of their intracellular uptake and interaction with DNA.

EXPERIMENTS and RESULTS: The synthesis of **1a~3a** and their Zn^{2+} complexes **1b~3b** was carried out and their cytotoxicity and cellular uptake activity against cancer cell lines (HeLa and A549 cells) and normal cell line (IMR-90) were determined on ICP-MS (inductivity coupled plasma-mass spectrometer), as shown in Fig. 2. It was found that the intracellular uptake of **1~3** is higher than that of BSH and BPA, possibly by the clathrin-endocytosis pathway including polyamine transporter system (PTS). Fig. 3 shows more potent BNCT effect of **^{10}B-2a**, **^{10}B-3a** **^{10}B-2b**, and **^{10}B-3b** than that of BSH and BPA.

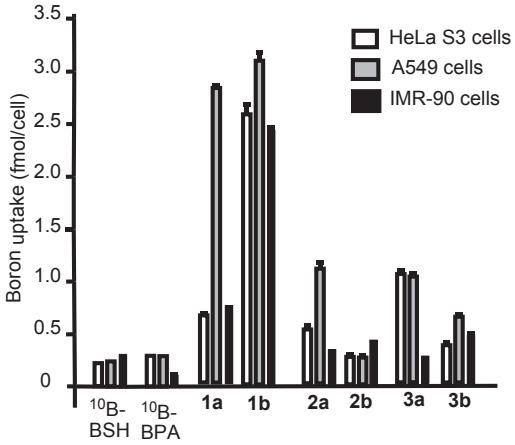

Fig. 2. The intracellular uptake **1~3** (30 μM) in HeLa S3, A549, and IMR-90 cells as determined on ICP-MS after the incubation with these drugs at 37 ºC for 24 hr. Data represent the mean ±SD of at least three replicates.

The design and synthesis of boron carriers that have higher intracellular uptake and more potent BNCT effect are now in progress.

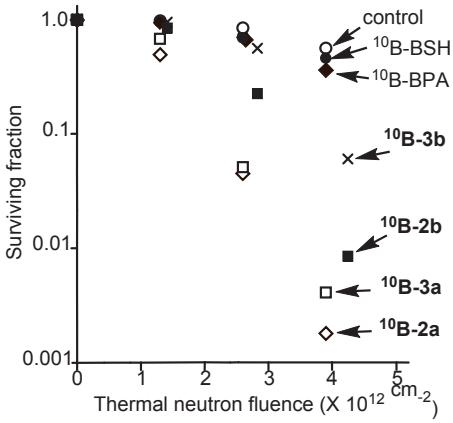

Fig. 3. Antitumor effect of ^{10}B-enriched BSH, BPA, **2a, 2b, 3a,** and **3b** (30 μM) against A549 cells upon irradiation with thermal neutron (averaged thermal neutron flux was 1.4 X 10^9 n/cm^2·s), as evaluated by a colony assay.

REFERENCES:

[1] a) R. F. Barth *et al.*, *Clin. Cancer Res.*, **11** (2005) 3987-4002. b) R. F. Barth *et al., Rad. Oncol*. **7** (2012) 146-166.
[2] M. Kitamura, *et al., Inorg. Chem.* **50** (2011) 11568-11580.
[3] H. Ueda, *et al., J. Med. Chem.* **64** (2021) 8523-8544

CO6-31 Elucidation of the effects of high dose rate radiation on normal and tumor tissues

Tsubasa Watanabe[1], Hiroki Tanaka[1], Minoru Suzuki[1]

[1]*Institute for Integrated Radiation and Nuclear Science, Kyoto University*

INTRODUCTION: Recent reports suggest that high-dose-rate irradiation, in which the dose rate is extremely high (1000 times or more) compared to the conventional radiotherapy dose rate (about 0.03 Gy/sec), suppresses side effects better than conventional irradiation and may have the same anti-tumor effect on tumors [1]. If side effects are indeed suppressed at ultra-high dose rates and anti-tumor effects remain unchanged, many conventional radiation therapies, especially X-rays, γ-rays, and proton beams, will be converted to high dose rates, and the position of neutron capture therapy will also change. This research plan will scrutinize the biological effects of ultra-high dose rates and clarify the differences compared to neutron capture therapy, focusing on biological responses and effects on tumors, to consider the future role of neutron capture therapy as a long-term cancer therapy. The goal of this fiscal year is to establish the irradiation environment necessary for this purpose.

EXPERIMENTS: Using an electron accelerator, we irradiate gafchromic films with pulsed electron beams and measure the dose per pulse. We constructed an irradiation system that can irradiate about 8-12 mice at a time.

RESULTS: The dose per pulse was sufficient for biological experiments, proving that experiments with high dose rates are possible. The irradiation system was constructed as shown in the figure (Figure 1 and Figure 2).

Figure1: Irradiation system of mice in a closed system in an acrylic box.

Figure2: The mouse is placed in the irradiation hole in the form of a radial projectile.

REFERENCES:

[1] Andrea Borghini *et al.* Int J Rad Biol 2022;98:127-135.

CO6-32 Theoretical Considerations on Reactor Production of Beta-Emitting Radionuclide ^{177}Lu for Targeted Radionuclide Therapy

K. Washiyama[1], T. Yamamura[2], T. Tabata[2], R. Okumura[2], K. Ogawa[3]

[1]*Advanced Clinical Research Center, Fukushima Medical University*
[2]*Institute for Integrated Radiation and Nuclear Science, Kyoto University*
[3]*Institute for Frontier Science Initiative, Kanazawa University*

INTRODUCTION: The medical use of radioisotopes (RIs) has already been applied since the discovery of RIs and radioactivity, and today, [^{18}F]F-FDG and [^{99m}Tc]Tc-labeled radiopharmaceuticals are recognized as important for nuclear medicine diagnosis. Although research and development of α-particles has been actively conducted in Japan in recent years from both basic and clinical aspects, there has been few research and development of reactor-generated nuclides in Japanese RI production over the past 20 years. For the future development of radionuclide therapy, it is important to conduct research on the development of radiopharmaceuticals based on the production and supply of β-radiopharmaceuticals using domestic nuclear reactors. PDRadiopharma will market ^{177}Lu-DOTATATE, a labeled drug for the treatment of somatostatin receptor-positive neuroendocrine tumors by the end of FY2021, and treatment has been provided to patients, but the supply source of the drug is entirely dependent on overseas countries. In March 2022, Novartis' ^{177}Lu-PSMA-617 was approved by the FDA as a targeted radioligand therapy for the treatment of advanced PSMA-positive metastatic castration-resistant prostate cancer, a disease that affects a large number of patients worldwide, so demand for ^{177}Lu is expected to increase worldwide. However, since the production of ^{177}Lu and the development of ^{177}Lu-labeled radiopharmaceuticals are not so active in Japan, it is possible that future domestic demand will not be fully met.

CONSIDERATIONS: ^{177}Lu can be produced by the ^{176}Lu(n,γ) ^{177}Lu reaction using thermal neutrons in a nuclear reactor with ^{176}Lu as a target. ^{176}Lu has a very high thermal neutron activation cross section, so irradiation in a reactor with high neutron flux can produce ^{177}Lu with high specific activity. However, the isotopes of natural ^{176}Lu is only 2.6%, so in practice, ^{176}Lu enriched to 70% or 98.5% is used. When the thermal neutron flux of reactors producing medical RIs, such as BR2 in Belgium and MARIA in Poland, is 3.0×10^{14}[1/cm^2/s], the specific activity reaches > 1,000 GBq/mg after 2 weeks of irradiation if more than 70% ^{176}Lu enriched isotope is also used (Figure 1). This value is close to the specific activity of 4,100 GBq/mg of no carrier added ^{177}Lu and is suitable for the development of antibody-labeled or peptide-labeled radiopharmaceuticals. In contrast, in the case of the hydraulic irradiation holes in the Kyoto University Research Reactor, the neutron flux is 1.6×10^{13} [1/cm^2/s], 1/20 of BR2, which is less, resulting in a specific activity of > 60 GBq/mg after 2 weeks of irradiation even using more than 70% ^{176}Lu-enriched isotopes. Based on this result, even if ^{176}Lu enriched isotopes are used, Japanese domestic reactors cannot produce ^{177}Lu with high specific activity, limiting its use to drugs that do not require very high specific activity, such as ^{177}Lu-EDTMP, a drug for bone pain palliation.

In contrast, ^{176}Yb can be used to produce ^{177}Lu indirectly by ^{176}Yb(n,γ)^{177}Yb→(β$^-$)→^{177}Lu reaction. Ytterbium and lutetium are rare earth elements, and their chemical properties are similar, but they can still be mutually separated using an extraction chromatography column, and target free ^{177}Lu can be purified. Because the isotope stability is 13.0%, so the use of an enriched isotope of ^{176}Yb is essential for the efficient production of ^{177}Lu even in the indirect production method.

CONCLUSION: This study revealed that a reactor with a high thermal neutron flux is necessary to produce ^{177}Lu with a high specific activity. In the case of domestic research reactors, the ^{176}Lu(n,γ) ^{177}Lu reaction cannot be used to produce ^{177}Lu with high specific activity, but the ^{176}Yb(n,γ)^{177}Yb→(β$^-$)→^{177}Lu reaction can be used to produce a target-free ^{177}Lu tracer by combining the chemical separation operation. In the future, for the sustainable production of reactor-generated β-emitters in Japan, development of radiopharmaceuticals, we will actually produce the β-emitting radionuclide ^{177}Lu, understand its production capacity and capability, and optimize the chemical separation technique.

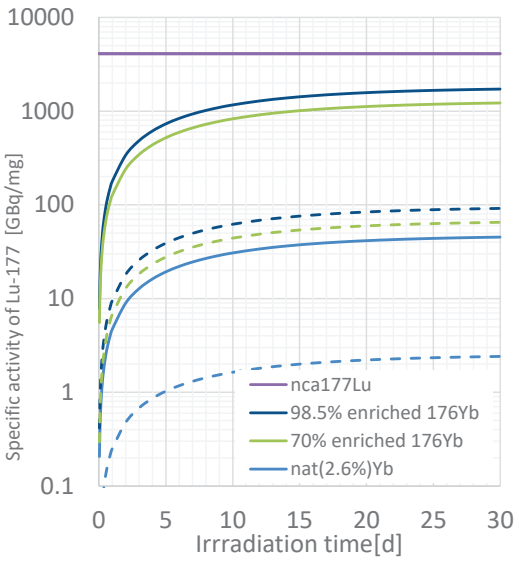

Fig. 1. Specific radioactivity [GBq/mg] of ^{177}Lu produced at $\varphi_{th}=3.0\times10^{14}$ (solid line) and 1.6×10^{13} (dashed line) [1/cm^2/s].

REFERENCES:

[1] W. V. Vogel *et al.*, Eur. J. Nucl. Med. Mol. Imaging, **48** (2021) 2329-2335.